Journal Pre-proof

Convection enhanced delivery of light responsive antigen capturing oxygen generators for chemo-phototherapy triggered adaptive immunity

Vishnu Sunil, Anbu Mozhi, Wenbo Zhan, Jia Heng Teoh, Chi-Hwa Wang

Please cite this article as: Sunil V, Mozhi A, Zhan W, Teoh JH, Wang C-H, Convection enhanced delivery of light responsive antigen capturing oxygen generators for chemo-phototherapy triggered adaptive immunity, *Biomaterials* (2021), doi: https://doi.org/10.1016/j.biomaterials.2021.120974.

This is a PDF file of an article that has undergone enhancements after acceptance, such as the addition of a cover page and metadata, and formatting for readability, but it is not yet the definitive version of record. This version will undergo additional copyediting, typesetting and review before it is published in its final form, but we are providing this version to give early visibility of the article. Please note that, during the production process, errors may be discovered which could affect the content, and all legal disclaimers that apply to the journal pertain.

Credit Author Statement

Vishnu Sunil: Conceptualization, Methodology, Investigation, Data Curation, Writing – Original Draft. Anbu Mozhi: Methodology, Investigation (H&E staining, TUNEL assay). Wenbo Zhan: Methodology, Formal Analysis, Investigation. Jia Heng Teoh: Methodology, Investigation (3D printing). Chi-Hwa Wang – Conceptualization, Supervision, Writing – Review and Editing, Funding Acquisition.

Convection Enhanced Delivery of Light Responsive Antigen Capturing Oxygen Generators for Chemo-phototherapy Triggered Adaptive Immunity

Vishnu Sunil[1], Anbu Mozhi[1†], Wenbo Zhan[2†], Jia Heng Teoh[1], Chi-Hwa Wang[1]*

[1]Department of Chemical and Biomolecular Engineering, National University of Singapore, 4 Engineering Drive 4, Singapore 117585, Singapore

[2]School of Engineering, King's College, University of Aberdeen, Aberdeen AB24 3UE, UK

[†]These authors contributed equally to this work.

[*]Corresponding Author:
Email: chewch@nus.edu.sg (C.H. Wang)

1. Keywords

Light-responsive; antigen-capturing; in-situ oxygen generation; 3D printing; hypoxia; adaptive immunity.

2. Abstract

In recent years, combination therapy has emerged as the cornerstone of clinical practice in treating glioblastoma multiforme. However, their ability to trigger and leverage the body's adaptive immunity has rarely been studied. Tumour heterogeneity, the presence of the blood-brain barrier, and an immunosuppressive tumor microenvironment play a crucial role in the 90% local tumor recurrence post-treatment. Herein, we report an improved combination therapy approach capable of stimulating an immune response that utilizes Light responsive antigen-capturing oxygen generators (LAGs). The engineered LAGs loaded with a non-genotoxic molecule, Nutlin-3a, and a photosensitizer, Protoporphyrin IX, can release the payload on-demand when exposed to light of a specific wavelength. The in-situ oxygen generation capability of LAGs enables tumor oxygenation enhancement, thereby alleviating the tumor hypoxia and enhancing the efficacy of chemo-photodynamic therapy. Furthermore, by modulating the surface properties of LAGs, we demonstrated that the tumor-derived protein antigens released can be captured and retained in-situ, which improves antigen uptake and presentation by the antigen-presenting cells. Dual drug-loaded LAGs (DD-LAGs) upregulated the expression of cell surface CD83 maturation and CD86 costimulatory markers on monocyte-derived-dendritic cells, suggesting intrinsic immune adjuvancy. In the presence of 3D printed hypoxic U87 spheroids (h-U87), DD-LAGs induced cancer cell death, upregulated IL-1β, and downregulated IL-10 resulting in CD3+, helper CD4+, and cytotoxic CD8+ proliferation. Finally, we have investigated convection-enhanced delivery as a potential route of administration for DD-LAGs. Our work presents a novel strategy to induce tumor cell death both during and post-treatment, thereby reducing the possibility of recurrence.

3. Graphical Abstract
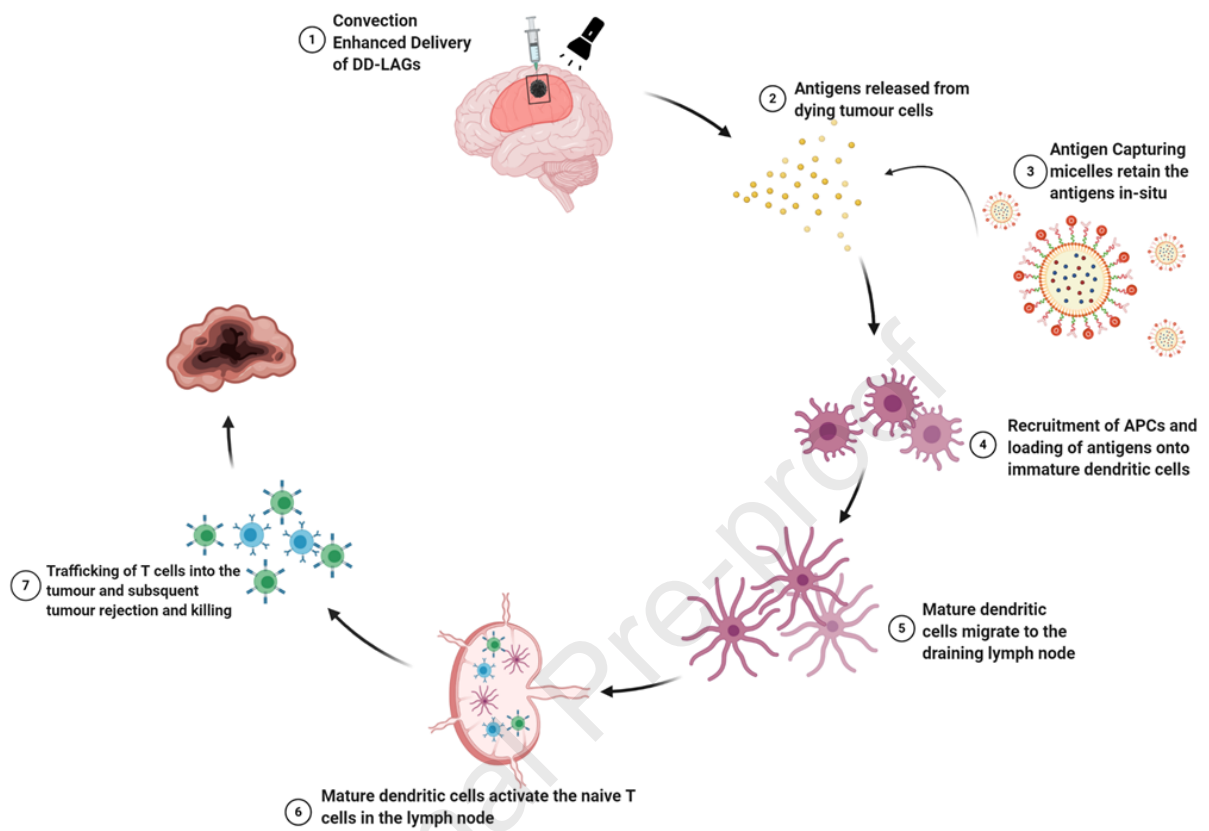
4. Introduction

The current standard of care for patients diagnosed with Glioblastoma multiforme (GBM), the most aggressive type of primary brain tumor with a dismal prognosis, includes maximal surgical resection in combination with radiation therapy and concomitant and adjuvant chemotherapy with Temozolomide (TMZ). In most cases, complete resection of the tumor is almost impossible due to the infiltrative nature of gliomas and their relative proximity to the eloquent cortex, thereby increasing the risk of early recurrence and tumor metastasis [1]. Hence, surgery and chemoradiation provide only a moderate improvement in long-term survival rates, with a median survival time approximately 18-24 months post-diagnosis [2]. Recently, Kadiyala et al. reported that in a cohort of 50 patients, an astounding 90% of the patients developed a local tumor recurrence. In contrast, 6% of the patients developed distant recurrence, and only 4% of the patients had no evidence of tumor recurrence three years post-treatment [3]. Although the oncologist's armamentarium has considerably expanded in the last two decades, chemotherapeutics remains the mainstay of treatment for most advanced cancers. However, for solid tumors, in particular, are rarely curative and cause significant off-target toxicity. On the other hand, immunotherapy is a promising alternative cancer treatment modality that can cause durable remission and eradication of solid and metastatic tumors through the activation of T-cell mediated immune response [4-8]. Despite the recent advances made in cancer immunotherapy, such as immune checkpoint blockader therapy [9, 10], cytokine therapy [11], and adoptive T cell transfer [12, 13], clinical studies have shown that many patients are not sensitive to immunotherapy with a relatively low objective response rate. The minimal clinical success of cancer immunotherapy could be attributed to several factors such as the heterogeneity of the tumor microenvironment (TME), individual variations, lack of production of neoantigens, insufficient presentation of these antigens to the antigen-presenting cells (APCs) in the draining lymph node, inadequate availability of T cells from the naïve repertoire, and substantial endogenous and treatment-induced immunosuppression [14]. It is reasonable to assume that a combination of chemotherapy and immunotherapy can cause significant tumor reduction and then successfully eliminate the tumor through immune mechanisms post-treatment. However, clinical data on the chemo-immunotherapy report otherwise. Patients treated with TMZ, particularly in dose-intensified regimens, exhibit an increase in the incidence of opportunistic infections and immunosuppression [15]. Low doses of chemotherapeutics that elicits poor apoptosis in tumour cells errs on the side of being immunologically bland and facilitate the development of immune tolerance [16-18]. Contrarily, when massive apoptosis occurs because of high chemotherapeutic dosage, the tolerogenic system might be overwhelmed, thereby activating an immune response [19]. However, myelosuppression, with both lymphopaenia and neutropaenia developing and resolving cyclically during treatment, is the major dose-limiting toxicity of many anti-cancer drugs and paradoxically, is detrimental to any potential immune response [20-22]. Since there is a scientific consensus on poor anti-cancer response of monotherapies, it is crucial to design combination regimens that represents a parallelism between cytotoxic and immunological effects that promotes synergistic therapeutic effect without any apparent toxicity both during and post-treatment.

Compared to chemotherapy, photodynamic therapy (PDT), an emerging minimally invasive clinical modality, can induce immunogenic cell death (ICD) through the generation of reactive oxygen species (ROS) using endogenous oxygen and irradiation of a potent photosensitizer [23-25]. ICD initiates a violent anti-tumor immune cascade response through the release of tumor-derived protein antigens (TDPAs) such as tumor-associated antigens (TAAs) and damage-associated patterns (DAMPs) as powerful supplements to the inadequate neoantigens [26-30], thereby stimulating an

4

"in-situ vaccine" to convert the "cold" immunosuppressive TME to a "hot" immunogenic TME. However, this promising treatment strategy's clinical application is severely hindered by its oxygen dependence in an inherently hypoxic TME [31, 32]. Unfortunately, around 50-60% of advanced solid tumors house heterogeneously distributed hypoxic cells, which are 2.8 to 3 times more drug-resistant than aerobic cells [33-36]. Furthermore, a hypoxic TME promotes the polarization of tumor-associated macrophages (TAMs) from M1-phenotype to M2-phenotype, thereby exhibiting pro-angiogenic and pro-tumorigenic properties and facilitating the evasion of tumor cells from the immune system [37-39]. In recent years, several strategies and concepts have been studied to modulate the hypoxia TME, such as direct oxygenation of tumors using perfluorocarbon (PFC) [40, 41], employing photocracking materials [42], use of red blood cells (RBCs) [43], and hemoglobin [44] as oxygen carriers and improving blood flow [45, 46]. However, all of these strategies have a litany of limitations, from the inadequate oxygen-carrying ability to deficiency and irregularity of microvessels within solid tumors leading to inequitable oxygen distribution within the tumor. Hence, we concluded that it is crucial to design an in-situ oxygen generating system that leverages the abundant hydrogen peroxide (H_2O_2) present in the hypoxic tumor tissue [47, 48].

Designing drug delivery systems (DDSs) programmed to leverage on synergistic combination effects is only half the solution, the delivery efficiency of these innovative DDSs to enable adequate therapeutic concentration at the target side is the other half that is crucial for their clinical translation. Wilhelm et al. reported that only an agonizing 0.7% of the administered nanoparticle dose reaches the solid tumor [49]. In fact, the delivery efficiency of systemically delivered DDSs to the brain would be even lower due to the presence of the blood-brain barrier (BBB) [50]. Diffusion controlled delivery methods such as implantation of drug-loaded wafers or intraneoplastic injection developed as alternatives to the traditional intravenous administration suffers from a poor volume of distribution [51] and have been associated with leakage and reflux around the injection site [52]. In contrast, convection-enhanced delivery (CED) utilizes convection bulk flow by maintaining a pressure gradient during interstitial infusion, resulting in intraparenchymal concentrations that are 100-fold greater and 1000- to 10000-fold greater compared intranasal and intravenous delivery, respectively [53-55].

In this work, we have designed light-responsive antigen capturing oxygen generators (LAGs) to enable the on-demand release of the therapeutic payload independent of the heterogeneous TME, to facilitate antigen capture and transport to the draining lymph node, and to aid in tumor oxygenation. This nanoparticle platform consists of three components: (i) an amphiphilic polymer brush composed of phosphatidyl ethanolamine (DSPE) and functionalized polyethylene glycol (PEG) connected through a ROS responsive thio-ketal (TK) linker, (ii) grafted with an oxygen-generating enzyme, catalase, and (iii) co-loaded with a non-genotoxic anti-cancer agent, Nutlin-3a (NUT), and a photosensitizer Protoporphyrin IX (PpIX). The fabricated delivery system was characterized and evaluated in ex vivo spheroid models to understand its oxygen generating, antigen capturing, and immune response modulating properties.

As shown in **Scheme 1**, CED is used to deliver the LAGs deep into the tumor bed, and when exposed to a light source of 630nm, LAGs would disassemble and release the payload in a triggered fashion. NUT causes tumor damage by inducing apoptosis or cell cycle arrest, promoting p53 stabilization which can reverse the immunological landscape towards anti-tumour immunity by releasing TAAs and modulating the immunological function of APCs through non-cell-autonomous activities [56-58]. On the other hand, PpIX elicits concurrent apoptosis and ICD, resulting in tumor regression and release of TAAs. Meanwhile, catalase converts the H_2O_2 to oxygen to modulate the hypoxic TME and enhance the PDT efficacy. The significantly enhanced availability of TDPAs due to the combination

5

therapy enables the maleimide groups to capture the TDPAs and transport them into the draining lymph node, thereby improving the presentation of TDPAs to the dendritic cells and subsequently

a.
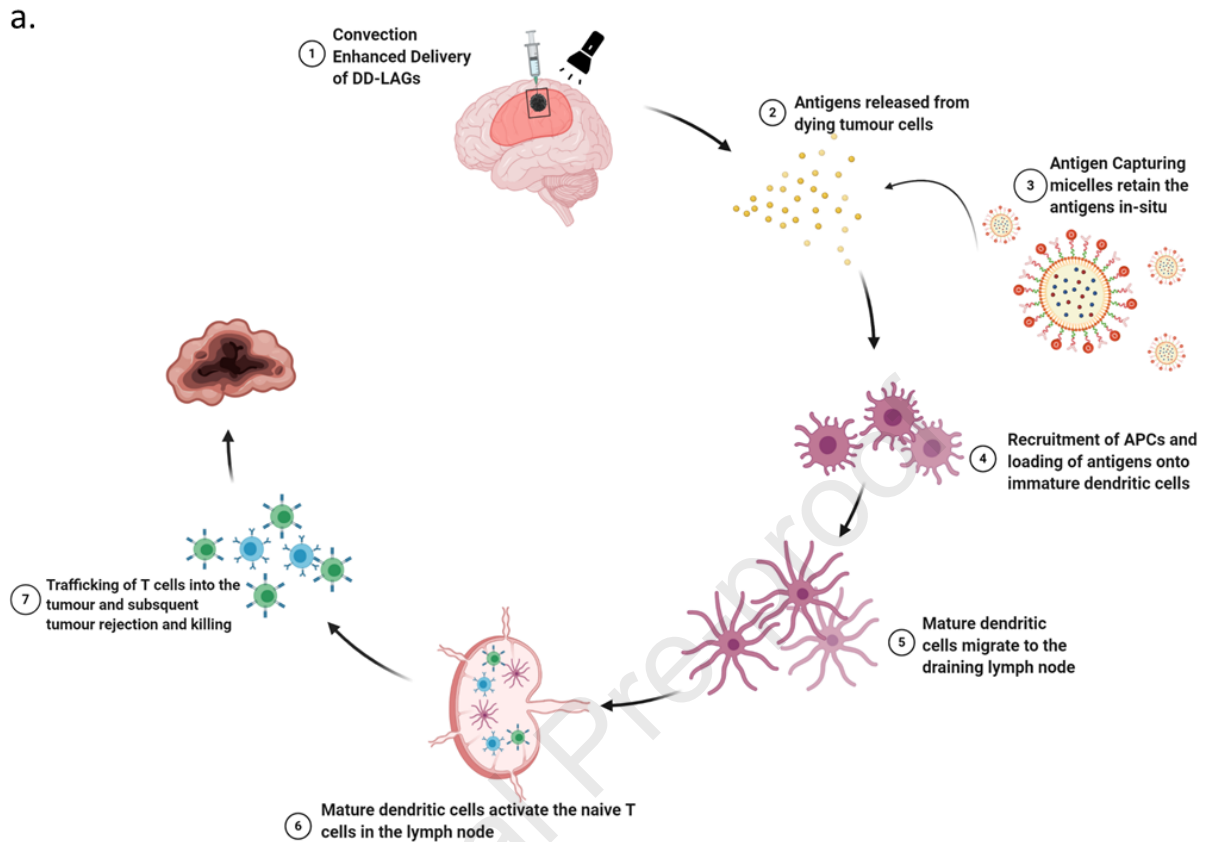
b.
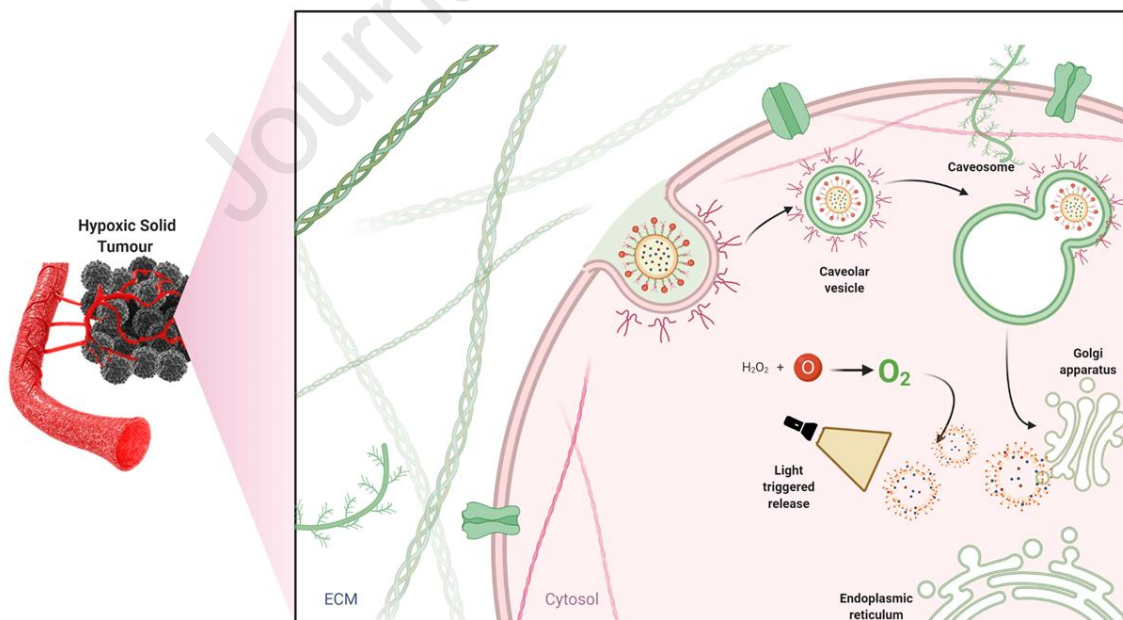
eliciting T-cell activation and proliferation.

Scheme 1. Schematic representation of utilizing DD-LAGs for chemo-phototherapy triggered anti-tumoural immunity. a) Convection enhanced delivery of DD-LAGs resulting in improved delivery efficacy and payload distribution for enhanced chemo-phototherapy; the released antigens are captured and retained in-situ; increased antigen uptake and presentation by APCs; subsequent

allogenic lymphocyte proliferation; T cell trafficking to tumor location to prevent a recurrence. b) Transcytosis mediated active tumor penetration and subsequent intracellular trafficking to the Golgi apparatus, followed by light-triggered payload release and in-situ oxygen generation by H_2O_2 decomposition.

5. Results and Discussion

5.1 Preparation and Characterization of LAGs

DSPE-PEG is a US FDA approved biomaterial that has been widely used to develop biocompatible and biodegradable delivery systems [59]. Several researchers have modified DSPE-PEG to fabricate micelles that are responsive to endogenous stimuli such as pH and glutathione [60]. However, it is difficult to achieve specific controllability due to the tumor heterogeneity. Hence, we developed a light-responsive analogue (DSPE-TK-PEG-MAL) bridged with a ROS cleavable thioketal linker that enables spatial and temporal control to achieve ON/OFF release kinetics (**Scheme S1, Supporting Information**). The products obtained at each step were systematically characterized by ^{1}H-NMR, electrospray interface mass spectrometer (ESI-MS) and FTIR to confirm their successful synthesis (**Figure S1-S6, Supporting Information**). Finally, dual drug-loaded LAGs (DD-LAGs) were prepared with Light Responsive Antigen Captors (LA), DSPE-TK-PEG-MAL, co-loaded with Nut3a, and PpIX by the film dispersion method, followed by grafting an oxygen generator, catalase, via a post-insertion thiol-maleimide click reaction [61]. Dual drug loaded light-responsive oxygen generators (DD-LG), which do not possess any free maleimide groups, were also fabricated using the same method. Similarly, Dual drug loaded antigen capturing oxygen generators (DD-AG), which do not possess the light-responsive thioketal linker, were prepared using the same method using commercially available DSPE-PEG-MAL.

The physiochemical characteristics of bare light-responsive antigen capturing oxygen generators (B-LAG), single drug-loaded analogues (NUT-LAG /PpIX-LAG), dual drug-loaded analogues (DD-LAG) are summarized in Table 1. The effect of each of the cargos on the physiochemical properties of DD-LAGs was studied using NUT-LAG and PpIX-LAGs (**Table S1 and S2, Supporting Information**). While the encapsulation of PpIX did not cause a significant change in the size of PpIX-LAG compared to B-LAG, the loading of NUT resulted in a size increase of ~48 nm. The encapsulation efficiency (EE%) of Nutlin-3a and PpIX was determined using high-performance liquid chromatography (HPLC). When payloads were loaded individually, EE% of NUT and PpIX were 94.09 ± 0.36 % and 28.29 ± 0.46, respectively, whereas 97.77 ± 0.82 and 64.77 ± 0.99 of NUT and PpIX were encapsulated when they were co-loaded into the LAGs.

As expected, both B-LAG and DD-LAG assembled into nanoparticles due to their amphiphilic nature in aqueous solutions, resulting in translucent solutions (**Figure 1a**). TEM, used to study the morphology and size distribution, showed a homogenous spherical structure for DD-LAGs with an average diameter of circa ~ 80 nm (**Figure 1b**). Whereas the average hydrodynamic diameter of B-LAG and DD-LAG measured using dynamic light scattering were 111.45 ± 0.47 nm and 122.43 ± 1.07 nm, respectively (**Figure 1c**). This discrepancy can be ascribed to the stretching property of PEG in aqueous environments. Since our studies were done in-vitro, the potential cellular responses of DD-LAGs in the physiological environment can be analyzed by studying their colloidal stability in appropriate cell culture media. DD-LAGs exhibited exceptional colloidal stability in α-MEM + 10% FBS media, with no significant increase in size even after two days (**Figure 1d**). This could be attributed to the presence of FBS, which is known to improve the colloidal stability of NPs [62]. Furthermore, the

DD-LAGs were stable in the stock solutions (PBS) for 15 days (**Figure S7, Supporting Information**). At pH 7.4, B-LAG and DD-LAG had zeta potentials of -7.09 ± 1.3123 mV and -7.34 ± 0.7474 mV, respectively (**Figure 1e**). The increase in size and zeta potential indicates the co-loading of the NUT and PpIX into the hydrophobic core of the nanoparticles. B-LAGs had an absorption maxima at 280 nm due to catalase, while the absorption spectra of DD-LAGs included the characteristic Soret band at 401 nm and Q band (450-630nm) of PpIX and the absorption maxima of NUT at 260 nm (**Figure 1f**). Similarly, B-LAGs showed no fluorescence, whereas DD-LAGs had a fluorescence maximum at 630nm (**Figure 1g**). The conformation of free catalase in B-LAGs and after drug loading in DD-LAGs was examined by circular dichroism (CD) (**Figure 1h**). Free catalase had a characteristic set of UV absorption bands in the far-UV CD spectrum region (<250 nm). The negative peaks at ~204 nm and ~228 nm and the positive peak at ~193 nm represent the protein's α-helical formation. In comparison, the negative peak at ~216 nm is typically attributed to the β-sheet conformation of the protein. Hence, the CD absorption spectra suggest that the secondary structure of catalase consisted of both α-helical and β-sheet peptides [63]. Catalase grafted onto B-LAGs and DD-LAGs had a similar CD spectrum compared to free catalase, thus proving that the grafting process did not affect the activity of catalase. The photodynamic property of DD-LAGs was evaluated by monitoring the fluorescence changes of a ROS-detecting probe, 2',7'-Dichlorofluorescin diacetate (DCFH-DA). When DD-LAGs were exposed to the light of 630nm for 4 minutes, the fluorescence of DCF at 535 nm increased by circa 5-fold (**Figure 1i**). The amount of conjugated catalase on LAGs was calculated to be 804 μg/ml using the Bradford assay. Furthermore, after 6 hours the catalytic activity of LAGs with/without proteinase K, an enzyme inactivator, significantly higher compared to free catalase using the standard Goth's method (**Figure 1j**). The superior oxygen generating capability of LAGs in the presence of H_2O_2 and proteinase K was demonstrated (**Figure 1k**). This significant difference in activity of free catalase and LAGs when exposed to proteinase K, can be attributed to PEG, which acts as a protective barrier by preventing opsonisation, while still providing access to the active sites of catalase [64, 65].

Table 1. Physicochemical characteristics of bare and loaded micelles used in this study.

Micelles	Size (nm)	PDI	EE (%) NUT	DLC (%) NUT	EE (%) PpIX	DLC (%) PpIX
B-LAGs	111.45 ± 0.47	0.228 ± 0.011	-	-	-	-
NUT-LAGs	159.54 ± 2.04	0.161 ± 0.014	94.09 ± 0.36	5.13 ± 0.01	-	-
PpIX-LAGs	123.50 ± 3.07	0.290 ± 0.026	-	-	28.29 ± 0.46	1.03 ± 0.014
DD-LGs	124.23 ± 2.45	0.288 ± 0.054	95.13 ± 0.91	5.18 ± 0.02	68.82 ± 0.82	2.50 ± 0.038
DD-AGs	119.74 ± 1.02	0.211 ± 0.013	94.61 ± 1.49	5.16 ± 0.04	64.77 ± 0.99	2.35 ± 0.061
DD-LAs	99.06 ± 3.20	0.266 ± 0.062	97.77 ± 0.82	5.33 ± 0.04	64.77 ± 0.99	2.35 ± 0.038
DD-LAGs	122.43 ± 1.07	0.237 ± 0.017	97.77 ± 0.82	5.33 ± 0.04	64.77 ± 0.99	2.35 ± 0.038

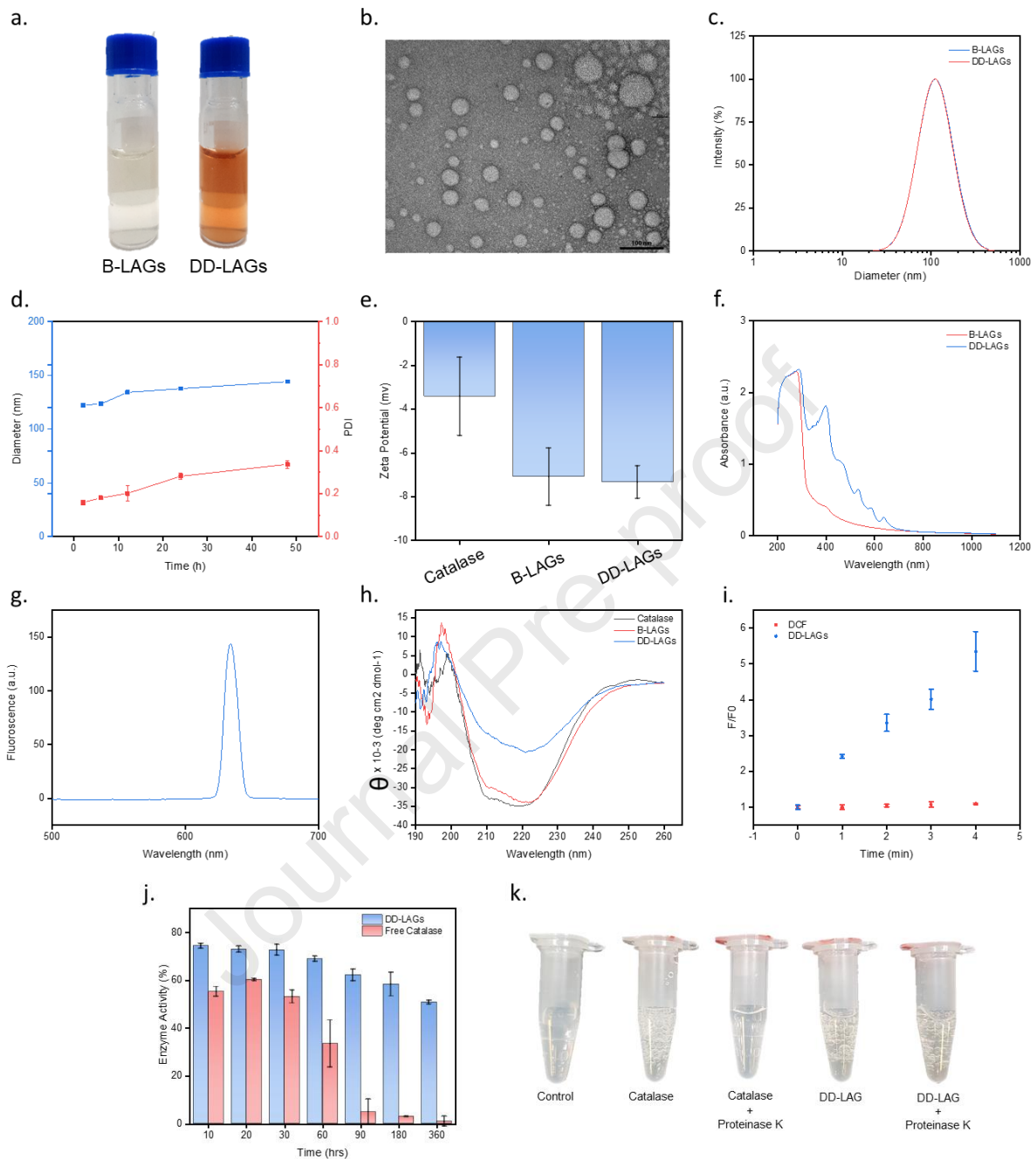DD-LGs (-malemide), DD-AGs (- thioketal linker), DD-LAs (-catalase)

Figure 1. In-vitro characterization of DD-LAGs. a) Images of the nanoparticle solutions, b) Representative TEM image of DD-LAGs in PBS. Staining was performed with 2% uranyl acetate (inset: Magnified image) (Scale bar: 100 μm), c) Hydrodynamic diameter distribution profile of B-LAGs and DD-LAGs, d) DLS data of DD-LAGs as a function of incubation time in α-MEM + 10% FBS media, e) Zeta potential of catalase, DD-LA, and DD-LAGs, f) UV/Vis absorption spectra, g) Fluorescence spectra, h) CD spectra of catalase, B-LAGs, and DD-LAGs, i) Generation of ROS determined by increased fluorescence intensity of DCF in the presence/absence of DD-LAGs as a function of photoirradiation time (630 nm, 130 mW cm^{-2}), j) Enzymatic activity of free catalase and DD-LAGs after proteinase K digestion as a function of time, k) Representative oxygen generation images of free catalase and DD-LAGs in the presence/absence of proteinase K. Error bars represent Mean ± SD (n ≥ 3).

9

5.2 On-Demand Customisable Light triggered Payload release

The proposed mechanism of photoactivation of DD-LAGs (**Figure 2a**) was confirmed using HPLC analysis (**Figure 2b**). When the solution of DD-LAGs was subjected to 630nm light irradiation (130 mW cm^{-2}) for 4 minutes, two elution peaks at 2.94 min and 12.52 min were observed, which was similar to that of NUT and PpIX, while no elution peaks were seen observed for the DD-LAG solution without photoirradiation. Similarly, DD-AG (TK negative group) showed no elution peaks with/without irradiation. The release of PpIX and NUT from DD-LAGs was dependent on the duration and intensity of irradiation (**Figure S8**, **Supporting Information**). Based on the results, a photoirradiation intensity of 130 mW cm^{-2} was chosen for subsequent experiments. The effect of a single pulse (4 min) and repeated pulses (8 min) on the release kinetics were assessed. Repeated irradiation enabled up to 4 triggerable events releasing 35.144 ± 0.35%, 3.84 ± 0.3%, 8.08 ± 0.7%, 0.804 ± 0.5% respectively (**Figure 2c**). We then studied the effect of the acidic tumor microenvironment on the triggered release profile of DD-LAGs and DD-AGs (**Figure 2d-g**). At pH 5, 18.04 ± 0.24 % of PpIX and 21.04 ± 0.002 % of NUT was released in the first 1 h, and when subjected to light (130 mW cm^{-2}, 4 min) at 0 hr, resulted in a release of 31.51 ± 0.56 % of PpIX and 34.51 ± 0.0056 % of NUT over the next 1 hr. Meanwhile, at pH 7.4, without irradiation, only 2.49 ± 0.45 % of PpIX and 6.48 ± 0.001 % NUT was released and with irradiation (130 mW cm^{-2}, 4 min) 25.56 ± 0.23 % of PpIX and 35.56 ± 0.002 % NUT was released in the same period of time. At the 8h time point, when exposed to light (130 mW cm^{-2}, 4 min), there was a similar triggered release for PpIX and NUT at both pH 5.0 and pH 7.4. These results suggest that LAGs can provide a customizable on-demand release of the payload. On the other hand, DD-AG had a similar release profile as DD-LAG at pH 5, but light exposure at 5 hr did not induce any cargo release. The representative disassembly

mechanism of DD-LAGs can be visualized using TEM (**Figure 2h**). DD-LAGs, which had an initial hydrodynamic diameter of 122.43 ± 1.07 nm, fell apart and formed smaller nanoparticles after each
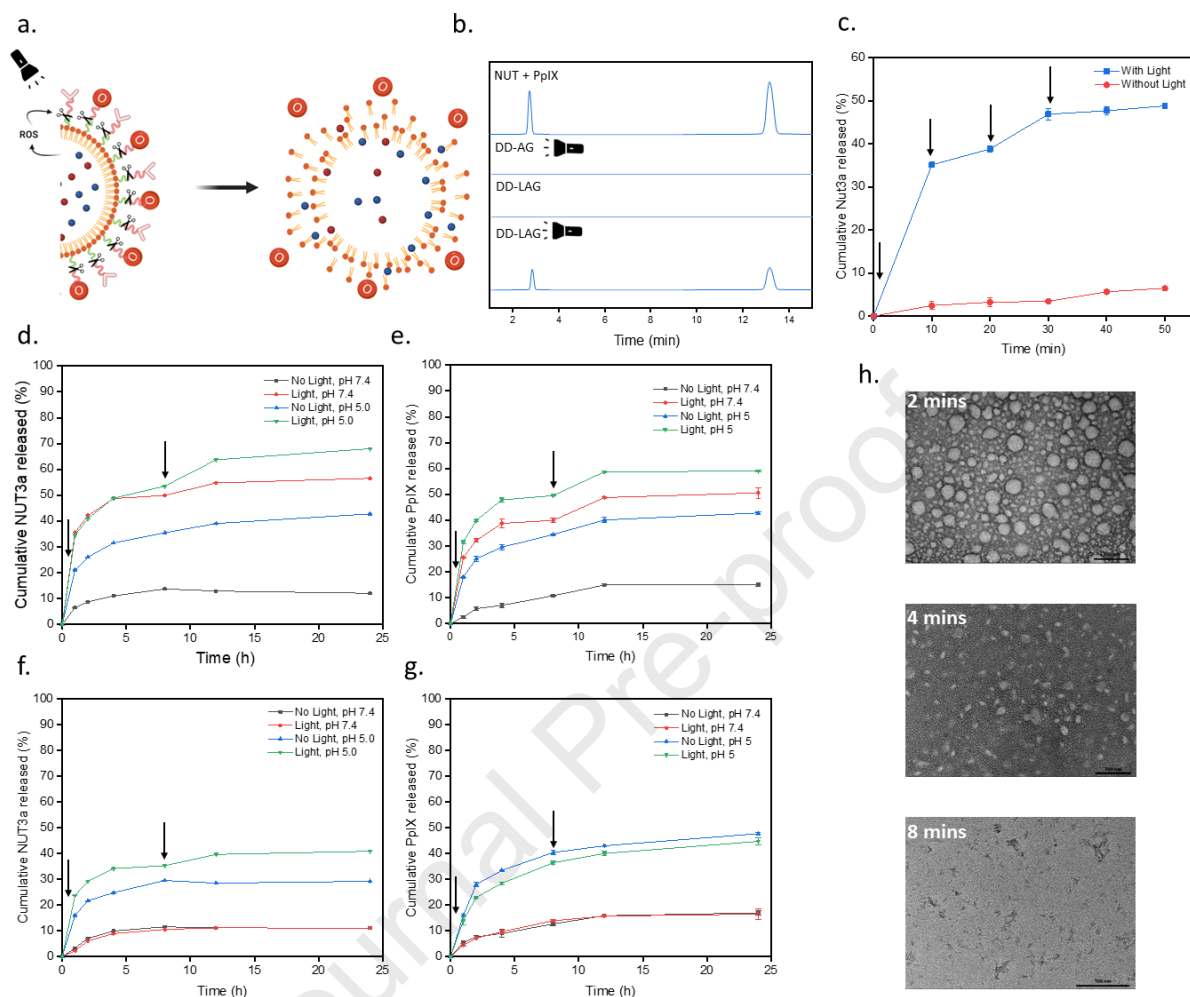
irradiation.

Figure 2. In-vitro study of on-demand customizable light-triggered payload release. a) Proposed mechanism of light-triggered payload release, b) HPLC profiles of free NUT, free PpIX, DD-AG, and DD-LAGs with/without light irradiation, c) Repeated light-triggered Nutlin-3a release (cumulative % of total); the arrows indicate irradiation (130 mW cm^{-2}, 4 min), d) Nutlin-3a released from DD-LAG at different pH solutions, e) PpIX released from DD-LAG at different pH solutions, f) Nutlin-3a released from DD-AG at different pH solutions, g) PpIX released from DD-AG at different pH solutions, h) TEM images of DD-LAGs at different photoirradiation times (Scale bar: 100 μm). Error bars represent Mean ± SD (n ≥ 3).

5.3 Anti-cancer activity of DD-LAGs in Hypoxic Spheroids

Since hypoxia is one of the main deterrents of effective cancer treatment, it is crucial to investigate the synergistic cancer cell killing effect of DD-LAGs in hypoxic U87 spheroids. But first, we assessed if the nanosystem would behave differently under normoxia and hypoxia conditions (**Figure S9, Supporting Information**). Thus far, spheroids developed are made up of an inner hypoxic core and an outer normoxic layer, which is far from the clinical reality. Most solid tumors have

12

heterogeneously distributed drug-resistant hypoxic cells, indicating inadequate vasculature, which could be further exacerbated by anti-angiogenic therapeutics [66]. This could prevent DDSs from reaching the quiescent cells deep within the solid tumor, thereby thwarting complete tumor eradication and increasing the possibility of recurrence. Hence, we 3D printed hypoxic U87 spheroids (h-U87) as a clinical comparator to evaluate our proposed therapy.

The use of drop-on-demand via 3D printing allows for the fabrication of tumor spheroids with uniform sizes (508.72 ± 19.46 μm). Compared to the manual deposition of cell suspensions (577.86 ± 149.79 μm), the consistency of cell deposition depends on the operator, and random errors will result in large variances of the shape and size of tumor spheroids formed (**Figure S10, Supporting Information)**. These factors may reduce the throughput of tumor spheroids and affect subsequent downstream characterization and therapeutic screening processes.

The cytotoxicity in h-U87 spheroids was evaluated by incubating free drugs, a combination of free drugs, dual drug-loaded light-responsive antigen captors (DD-LA, without catalase), and DD-LAG with different concentrations (NUT concentration 0.25, 2.5, 5, 10, 20, 40 μg/ml) with/without light for 24 hours (**Figure 3a, b, c**). The Chou-Talalay isobologram method was used to evaluate drug combinations. The calculated combination index (CI) was 0.567 and is a quantitative descriptor for synergistic (CI<1), additive (CI=1), and antagonistic effects (CI>1). The cytocompatibility of B-LAGs was studied on 3T3 cells (**Figure S11, Supporting Information)**.

The growth inhibitory effect of DD-LAGs over 8 days was also studied (**Figure S12, Supporting Information)**. All the treatment groups except DD-LAGs produced an initial reduction in tumor volume but enabled tumor proliferation after ~4 days. Interestingly, compared to the other treatment groups, DD-LAGs + Light did not cause any undesirable multicellular detachment, which forms metastatic tumors [67].

This result was further confirmed using a live/dead assay, in which the live cells are stained in green while dead cells emit red fluorescence. The untreated h-U87 spheroids showed negligible dead cells, mostly due to the necrotic core (**Figure 3d**).

We then studied the various cell killing mechanisms involved in the observed cytotoxicity. It is well known that the generation of ROS and loss of mitochondrial membrane potential (Δψm) are the mainstays of effective photodynamic therapy. Hence, we evaluated the intracellular ROS generation of DD-LAGs using DCFH-DA (**Figure S13, Supporting Information**) and its effect on the Δψm using the JC-1 assay (**Figure S14, Supporting Information**). Compared to the free drugs, DD-LAGs + Light showed a high green fluorescence signal in h-U87 cells. This suggests that catalase plays an important role in enhancing ROS generation by converting H_2O_2 to oxygen. Notably, the DCF fluorescence signal of cells treated DD-LAs was weaker than that of DD-LAGs. This might be due to the antioxidative mechanism of catalase [68]. Moreover, the DD-LAGs + Light treated group had the lowest Δψm, represented by the green fluorescence of the monomers in the cytosol, compared to the groups treated with equivalent molar ratios of free payloads and DD-LAs, which emit red fluorescence due to the accumulation of JC-1 aggregates in the mitochondria.

Histological sections of h-U87 spheroids treated with the different formulations with/without light were studied to evaluate cell morphology changes (**Figure 3e**). Cells in spheroids of the control group appeared normal, with an intact extracellular matrix and abundant cytoplasm having a well-defined nucleus. The spheroids treated with free drugs, a combination of NUT and PpIX, DD-LAs and DD-LAGs showed a large nucleus and a scanty cytoplasm. In contrast, cells in spheroids treated with DD-

LAGs + light showed disrupted extracellular matrix with an irregular nucleus, and many cells lacked genomic nucleus.

The stages of apoptosis in h-U87 spheroids were evaluated using the Annexin-V/FITC assay. After just 6 hours of incubation, there was a relative increase in annexin V binding and PI on DD-LAG + Light treated spheroids, resulting in 16.91% of necrosis and 13.05% of late-stage apoptosis (**Figure 3f**). While free payloads and DD-LAs had predominately healthy cells. This was further verified using TUNEL staining (**Figure S15, Supporting Information)**.

DD-LAGs, when exposed to light (130 mW cm^{-2}, 4 min), caused a significant decrease in G1, S, and G2/M phase compared to DD-LAGs without light (**Figure S16, Supporting Information**). This could be due to the triggered release of the encapsulated NUT [69]. Contrary to its proposed mechanism of action as a non-genotoxic antagonist of MDM2, these results suggest that NUT has a secondary role as a DNA-damaging agent, inducing p53-mediated apoptosis and cell cycle arrest [70]. While activated PpIX triggers apoptotic pathways through both direct (cell death) and indirect (vascular damage) mechanisms [71].

The extent of immunogenic cell death (ICD) was evaluated by the calreticulin exposure and high-mobility group box 1 (HMGB1) release from h-U87 cells. DD-LAGs + Light treated h-U87 cells induced the highest amount of HMGB1 release (**Figure 3g**). Furthermore, a stronger green fluorescence was observed for DD-LAGs + Light treated h-U87 cells compared to free NUT, free PpIX, a combination of NUT and PpIX and DD-LAs (**Figure 3h**).
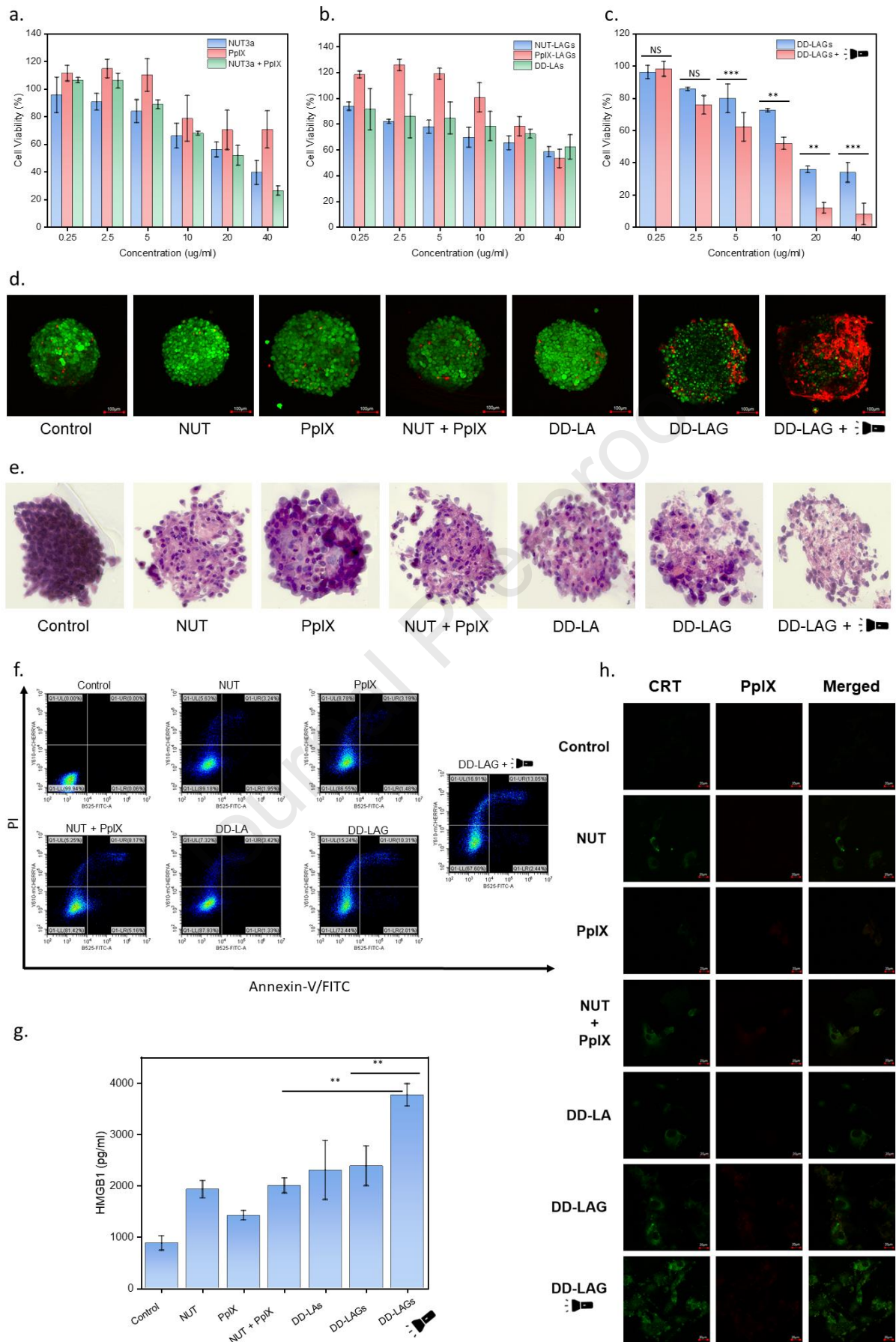
15

Figure 3. In-vitro anticancer activity in h-U87 spheroids. a-c) Cytotoxicity of free NUT, free PpIX, a

combination of free NUT and free PPIX, DD-LAs and DD-LAGs with/without light (130 mW cm^{-2}, 4 min) at different concentrations on h-U87 spheroids after 24 h of incubation, d) Representative images of live/dead viability assays in h-U98 spheroids treated with different formulations for 6 h (Scale bar: 100 μm), e) Hematoxylin and Eosin (H&E)-stained sections of h-U87 spheroids treated with different groups for 6 h, f) Flow cytometry analysis of h-U87 spheroids apoptosis by various formulations for 6 h using the Annexin V-FITC/PI staining, g) Detection of extracellular release of HMGB1 from h-U87 spheroids after 6 h of incubation with different groups, h) Confocal images of CRT expressed on the surface of h-U87 cells after treatment with different formulations for 6 h (Scale bar: 20 μm). Levels of significance were set at the probability of *p < 0.05, **p < 0.01, ***p < 0.001. Error bars represent Mean ± SD (n ≥ 3).

5.4 Enhanced Cellular Uptake and Penetration of DD-LAGs

The cellular uptake of free PpIX, DD-LA, and DD-LAG was studied in hypoxic U87 cells using confocal microscopy and flow cytometry. The fluorescence of PpIX was used to quantify and analyze the uptake of the nanoparticles. The results show that after 6 h of incubation, the cell uptake of DD-LAGs was greater than that of free PpIX and DD-LA (**Figure 4a and 4b**). Interestingly, the presence of catalase increased the cellular uptake of the nanoparticles. Flow cytometric results also showed greater uptake of DD-LAGs in hypoxic U87 cells (**Figure 4c and 4d**). A nearly 2-fold increase in the cellular uptake was observed when comparing the DD-LAGs to free PpIX.

We further mapped out the cellular internalization route and subsequent intracellular localization of DD-NP in hypoxic U87 cells. Both confocal and flow cytometry data suggested an energy-dependent internalization as the cellular uptake of DD-LAGs was significantly inhibited at 4 °C (**Figure S17, Supporting Information**). Similarly, the cell uptake of DD-LAGs was blocked by the dynamin inhibitor (dynasore) and was not affected by the macropinocytosis inhibitor (wortmannin) (Figure S13), suggesting either clathrin-mediated endocytosis or caveolin-mediated endocytosis [72]. Further investigation revealed that the cellular uptake was unaffected by a clathrin-mediated endocytosis inhibitor (chlorpromazine) and was by a caveolar inhibitor (genistein) (**Figure S17**). Hence we can infer that the internalization of DD-LAGs into the cells occurs predominately by caveolae-mediated endocytosis.

To further map out the endocytic pathway of DD-LAGs, the hypoxic U87 cells were stained with a lysosome marker (Lysotracker Green) and a macropinosome marker (^{RhoB}dextran, 70kDa). Poor Person correlation coefficients (PCC) of 0.39 and 0.51 were obtained using the internalized DD-LAG fluorescent signals co-localized with lysosomes and macropinosomes, respectively (**Figure S18, Supporting Information**). In contrast, after 6 h of incubation, a relatively high PCC (0.86) was obtained as DD-LAGs slowly co-localized with the Golgi tracker, whereas a low PCC (0.45) was obtained using signals of DD-LAGs co-localized with the Endoplasmic reticulum tracker, suggesting that most of the internalized DD-LAGs were trafficked to the Golgi apparatus (**Figure S18**). These results indicate that DD-LAGs were predominantly transported to the Golgi apparatus through caveolae-mediated endocytosis.

Furthermore, the penetration of DD-LAGs into solid tumors was investigated using h-U87 spheroids. The penetration capability was evaluated by measuring the fluorescence of the loaded PpIX using confocal microscopy (**Figure 4e**). These images were then converted into surface plots using ImageJ (**Figure 4f**). h-U87 spheroids treated with DD-LAG showed the highest PpIX fluorescence intensity and relatively uniform distribution compared to free PpIX and DD-LA. Sectioning of the h-U87 spheroid images using the Imaris software revealed that DD-LAGs achieved an exceptional

penetration depth of ~300 μm compared to the poor penetration efficiency of free PpIX (<100 μm) and DD-LAs (~200 μm).

The enhanced penetration of DD-LAGs could be due to transcellular transport or paracellular diffusion through the extracellular matrix. We pre-treated the h-U87 spheroids with either genistein or Exo1. This blocked the penetration of DD-LAGs into the spheroids and limited them to the spheroids' outer boundaries (**Figure 4g**). Since transcytosis is associated with cellular uptake on one end and exocytosis on the other end, the penetration of DD-LAGs into solid tumors could be via transcytosis that depends on caveolae-mediated endocytosis and exocytosis. Furthermore, the exocytosis-dependent transcytosis of DD-LAGs was studied using an 'infection' method, which involves several passes of incubating treated h-U87 cells with freshly seeded h-U87 cells in fresh media (**Figure 4h**). It is evident that PpIX signal is present in the cells on coverslips (2) and (3), suggesting that the DD-LAGs internalized by the cells on the coverslip (1) was exocytosed into the medium and subsequently taken up by the cells present on coverslips (2) and (3).

The multidrug efflux pump P-glycoprotein (P-gp) acts as a "hydrophobic vacuum cleaner" by pumping out foreign substances out of the cells and is known to contribute to multidrug resistance in about half of human cancers [73]. To confirm whether DD-LAGs are subjected to P-gp efflux, we pre-treated the h-U87 cells with a P-gp inhibitor (tariquidar) (**Figure 4h, i**). Both the exocytosis and intracellular transfer of DD-LAGs were unaffected by tariquidar, but Exo1 significantly inhibited both the behaviors.

These results confirm the solid tumor penetration of DD-LAG involving a transcytosis mechanism that depends on a rapid non-degenerative endocytic pathway and its adequate endocytosis.
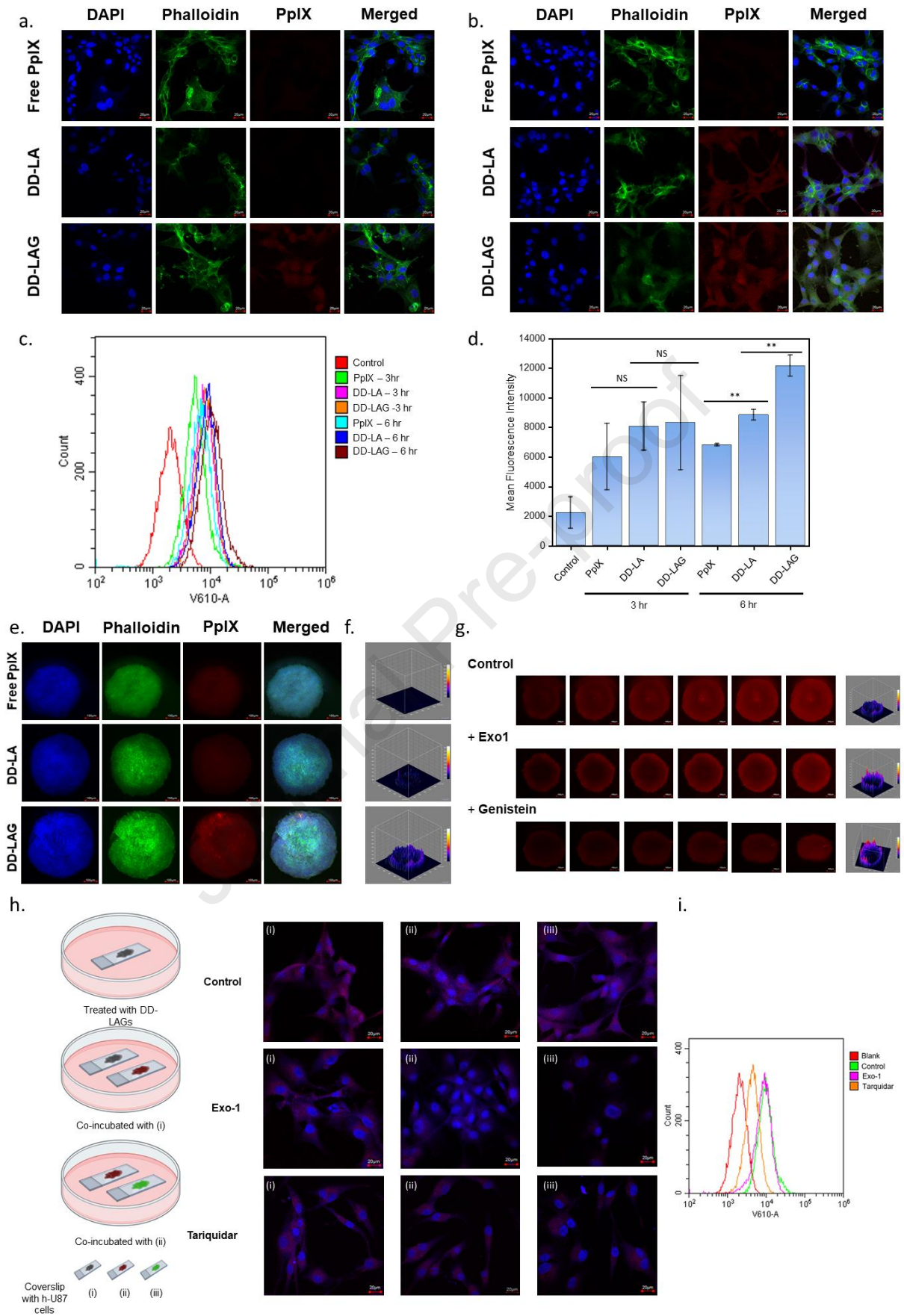
Figure 4. Cell uptake and Penetration of DD-LAGs into h-U87 spheroids. Cell uptake of free PpIX, DD-LA, and DD-LAGs after a) 3 h and b) 6 h of incubation with h-U87 cells (Scale bar: 20 μm), c) Flow

cytometry analysis of cell uptake by measuring PpIX fluorescence intensity, d) Mean Fluorescence Intensity of the cellular uptake of the different groups after 3 h and 6 h of incubation with h-U87 cells, e) Confocal microscopy observations of free PpIX, DD-LAs and DD-LAGs penetrating h-U87 spheroids after 6 h of incubation (Scale bar: 100 μm), f) Surface plot images of h-U87 spheroids treated with free PpIX, DD-LAs, and DD-LAGs, g) Effects of caveolae-mediated endocytosis inhibitor genistein and Exo1 on the DD-LAGs penetration into h-U87 spheroids (Scale bar: 100 μm). The spheroids were pre-treated with genistein or Exo1 for 1 h and then incubated with DD-LAGs for 6 h, h) Confocal images depicting the Intracellular transfer of DD-LAGs. The coverslips were treated with Exo1 and Tariquidar for 1 h before incubation with DD-LAGs (Scale bar: 20 μm), i) Flow cytometric analysis to study the effect of Exo1 and Tariquidar. Levels of significance were set at the probability of $*p < 0.05$, $**p < 0.01$, $***p < 0.001$. Error bars represent Mean ± SD (n ≥ 3).

5.5 Ex-vivo Antigen Capturing potential and APC Recruitment

Having proven the excellent capability of DD-LAGs to generate TDPAs, we sought to test our hypothesis that the surface chemistry of DD-LAGs would affect its antigen capturing potential [74]. As a negative control, dual drug-loaded light-responsive oxygen generators (DD-LG, -maleimide) were used. DD-LAGs and DD-LGs were incubated with treated h-U87 cell lysates ex vivo. Both the hydrate size and zeta potential of DD-LAGs changed after incubation, indicating successful TDPA capture (**Figure 5a, b**). In comparison, the size and zeta potential of DD-LGs remained unchanged after incubation. This suggests that the maleimide groups present in DD-LAGs enable the capture of the released proteins through stable thioether bonds.

5.6 Immunostimulative Effect of DD-LAGs in the absence/presence of h-U87 Spheroids

The next step of eliciting an effective immune response is the maturation of the recruited iDCs, which would subsequently activate the naïve T cells in the draining lymph node. A complete package of TDPAs, cytokines, and costimulatory signals are required to prevent T-cell anergy and resulting immune tolerance [75]. The immunostimulatory properties of DD-LAGs were evaluated by studying the expression of a costimulatory molecule C86 and a maturation marker CD83 on monocyte-derived dendritic cells (Mo-DCs) using flow cytometry (**Figure 5c, d**). Untreated Mo-DCs that presented low CD83 expression were considered as iDCs. Compared to the control (TNF-α and IL-1β), free NUT free PpIX, and a combination of free NUT and free PpIX had only a marginal effect on CD86 and CD83 expression. On the other hand, DD-LAGs produced a statistically significant ~6 fold increase in CD83 expression and a ~10% increase in CD86 expression. This suggests that LAGs exhibit intrinsic adjuvancy and does not require any additional adjuvants to cause DC stimulation.

Furthermore, we evaluated the immunostimulation of monocyte-derived dendritic cells after exposure to h-U87 spheroids. As expected, DD-LAGs can significantly upregulate the CD83 and CD86 expressions, both in the absence/presence of h-U87 spheroids (**Figure 5e, f**). Interestingly, h-U87 spheroids had only a slight effect on the C83 expression but promoted a considerable increase in the C86 expression. This might be because of the "eat me" signals released by the apoptotic cells into the culture media, which might be engulfed by DCs, resulting in a partially stimulated status [76] [77].

Additionally, the immunomodulating effects of DD-LAGs were studied by measuring the secretion levels of IL-1β (proinflammatory/immunostimulator) and IL-10 (anti-inflammatory/immunosuppressive) cytokines by DCs. h-U87 spheroids alone elevated the IL-1β and IL-10 cytokines levels by the Mo-DCs (Figure 5g,h). Unlike other cancers, studies have shown that glioblastoma is not a source of IL-10 but can stimulate Mo-DCs to produce IL-10 [78]. Noteworthy,

DD-LAGs induced downregulation of IL-10 and a significant parallel upregulation of IL-1β in the presence of h-U87 spheroids. The downregulation of IL-10 cytokine, associated with reduction of regulatory T-cell (T$_{reg}$) population and subsequent prevention of T-cell anergy [79], proves that DD-LAGs can potentially modulate the immunosuppressive TME. Despite the cognitive dissonance among scientists regarding the role of IL-1β as an immunostimulator and antitumorigenic, several previous studies have shown its immense potential as an "endogenous adjuvant" due to its role in T-cell priming, maturation and activation of APCs [80] and expansion of naïve and memory CD4$^+$ T cells
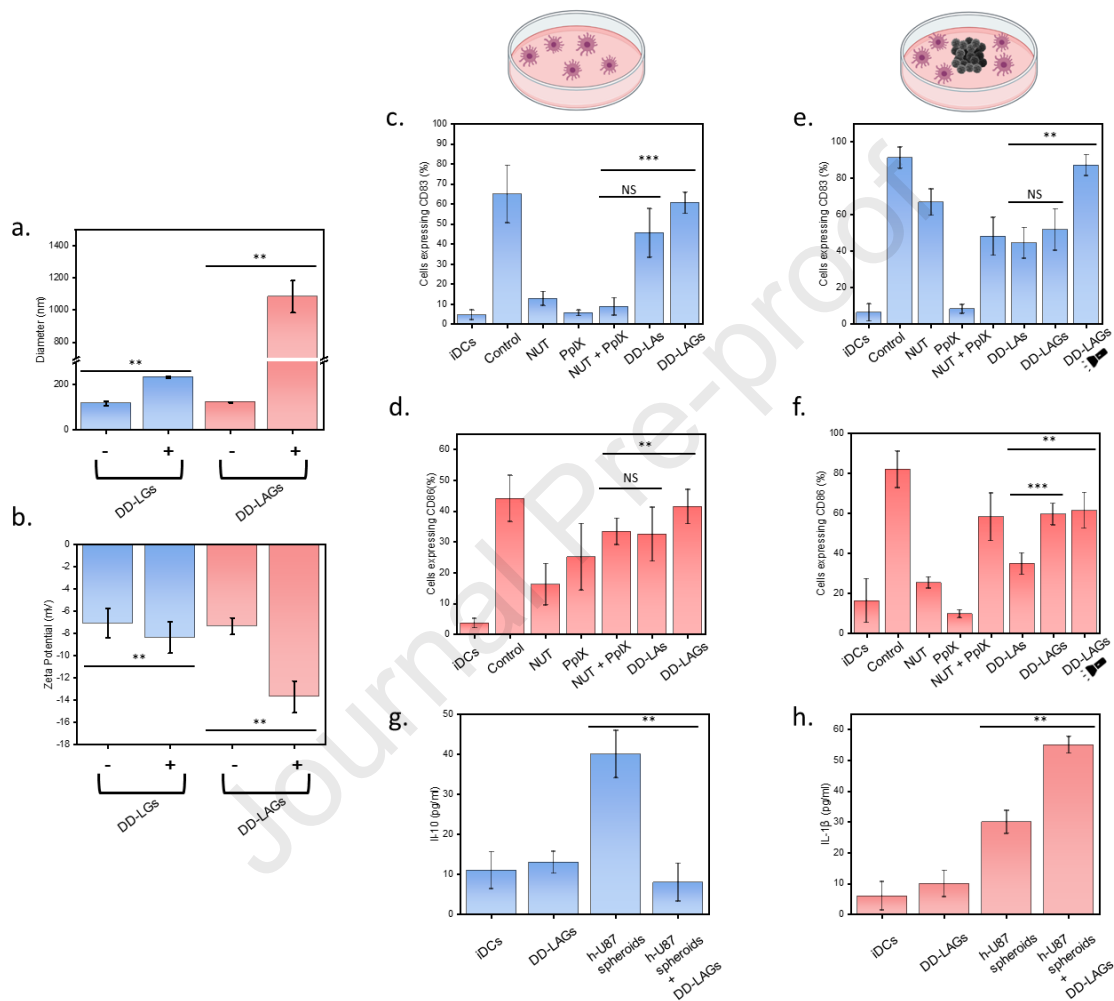
[81].

Figure 5. Antigen Capturing and DC Stimulation. The change in a) The hydrodynamic diameter and b) zeta potential of DD-LGs and DD-LAGs following antigen capture. Percentage of Mo-DCs expressing a) CD83 and b) CD86 after incubation for 24 h with different formulations. Percentage of Mo-DCs expressing e) CD83 and f) CD86 in the presence of h-U87 spheroids after incubation with various groups for 24 h, g-h) Cytokine expression. Levels of significance were set at the probability of *p < 0.05, **p < 0.01, ***p < 0.001. Error bars represent Mean ± SD (n ≥ 3).

5.7 T-cell Differentiation and Proliferation

The penultimate step of effective immunotherapy is the T-cell proliferation and priming. We accessed the effect of DC maturation on T-lymphocyte proliferation by culturing the stimulated DCs (both in the absence/presence of h-U87 spheroids) with CellTrace Violet labeled allogeneic

peripheral blood lymphocytes (PBLs) (**Figure 6a**). A flow cytometer is used to measure the progressive dilution of the dye with each cycle of proliferation, and when the proliferation index (PI) was greater than 3, the proliferation index was considered positive [82]. As seen in **Figure 6b**, the free payloads and their combination had almost no effect on the percentage of proliferating cells. Contrastingly, DCs stimulated with DD-LAGs could induce T-cell activation and proliferation. This could be due to the increased p53 stabilization on DCs resulting from the delivery of Nut3a [83]. Few studies have shown the promoter region of interleukin 12 (IL-12) and the role of p53 stabilization in the enhancement of the ability of DCs to prime T cells. **Figure 6c** shows the capacity of stimulated DCs in the presence of h-U87 spheroids to elicit CD3$^+$ proliferation and subsequent priming into helper CD4$^+$ and cytotoxic CD8$^+$ subsets. We assume that the enhanced antigen capture and DC maturation caused by DD-LAGs + Light treated h-U87 spheroids enable the priming of CD3$^+$ cells into helper CD4$^+$ (**Figure 6d**)and cytotoxic CD8$^+$ T lymphocytes (**Figure 6e**).
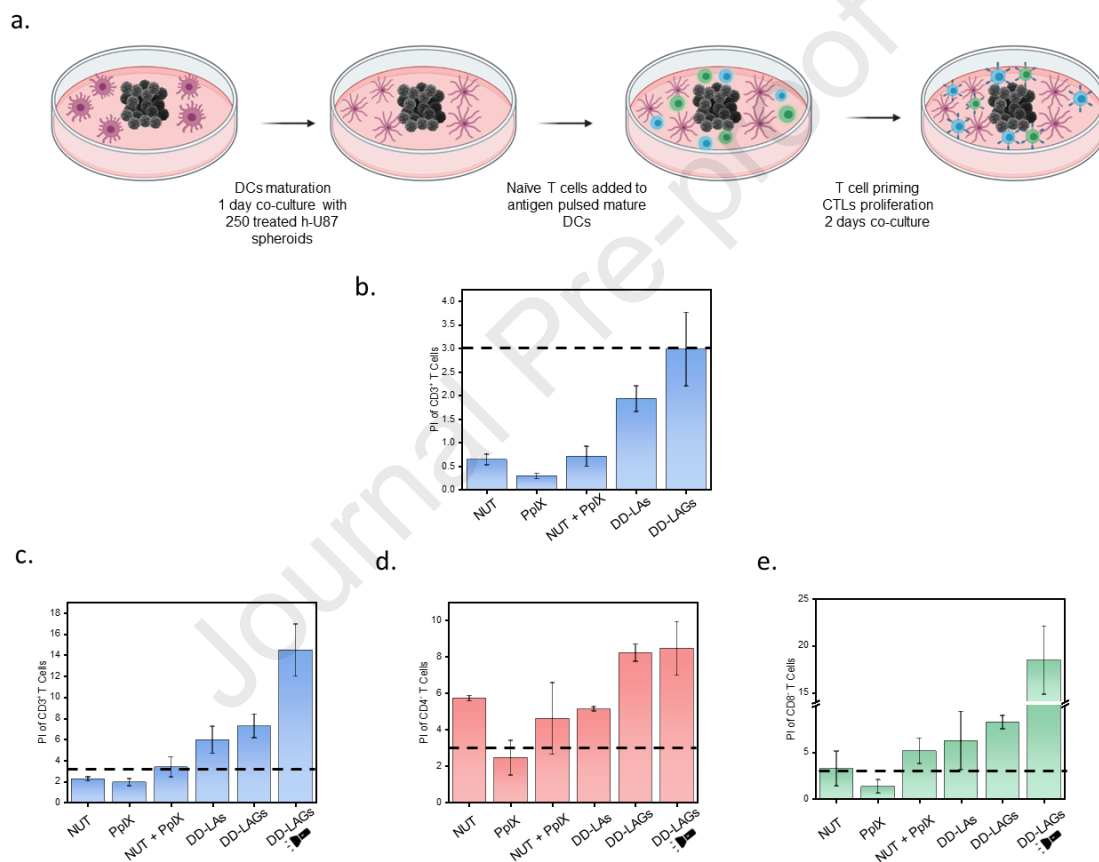

Figure 6. T-cell proliferation in the absence/presence of h-U87 spheroids. a) Overview of the ability of DD-LAGs to elicit the immune response of DCs in the presence of h-U87 spheroids, b) Proliferative response of CD3$^+$ T cells was analyzed through T-cell-DC co-culture for 24 h, c) CD3$^+$ T cells, d) CD3$^+$ CD4$^+$ T cells, e) CD3$^+$ CD8$^+$ T cells proliferation response in T-cell-h-U87 spheroid-DC co-culture for 48 h. Levels of significance were set at the probability of *p < 0.05, **p < 0.01, ***p < 0.001. Error bars represent Mean ± SD (n ≥ 3).

5.8 Delivery Efficacy and Payload Distribution

Figure 7 compares the NUT and PpIX concentrations in each tissue compartment in the treatments using DD-AG and DD-LAG with/without light irradiation, respectively. The treatment duration is set as 3 hours, comparable to the time window of intravenous administration. The most effective delivery of both NUT and PpIX in ECS and IVS are found for the therapy in which the light irradiation

enhances DD-LAG release. Results show that DD-AG and DD-LAG without light would result in comparable intracellular drug concentrations in the simulated time window. In contrast, the intracellular concentrations can be slightly increased when light is used to enhance the dynamics of drug release from nanoparticles.

Results shown in **Figure 7** demonstrate that the combination of DD-LAG + light can increase the concentrations of both NUT and PpIX in all the tissue compartments, including blood, tumor tissue, and tumor cells. This improved drug delivery outcome would indicate better treatment efficacy. However, further quantitative analysis shows that the difference in the time course of tumor cell density is trivial between these three treatments in the simulated time window. The small difference in the NUT and PpIX intracellular concentration, as shown in **Figure 7**, could be the potential reason. As compared to the simulated time window that is 3 hours in this study, the drug cell-uptake and tumor cell killing are show-rate dynamics processes that may take hours to days [84, 85]. Given this difference in the dynamic process rate, the drug delivery duration commonly used in intravenous administration, such as the 3-hour infusion, could be insufficient for CED treatment. A longer CED infusion duration of up to 5 days has been applied in the clinical trial where free drugs were used [86]. However, there is a lack of either preclinical or clinical data for nanoparticles. This requirement on CED infusion duration would need to be further validated.

Due to the lack of experimentally measured data available for NUT and PpIX, the relevant parameters in the governing equations of cell-uptake and immunotherapy are estimated based on doxorubicin, which has a similar molecular weight. Therefore, modeling results presented in this study can only serve for the qualitative comparison purpose. Further experimental measured data of
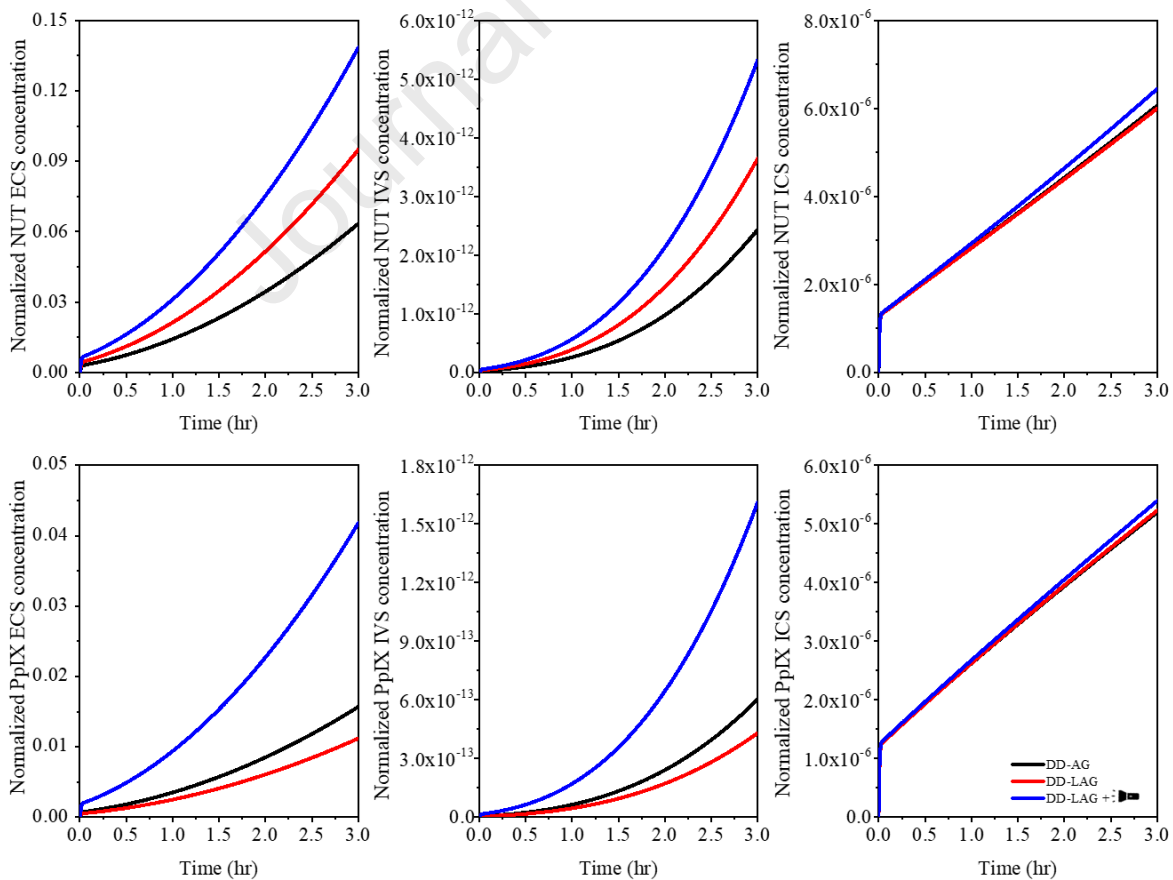
NUT and PpIX properties will be needed to relax this limitation for a quantitative study.

Figure 7. The time courses of NUT and PpIX concentration in blood, tumor extracellular space, and tumor cells under different delivery conditions. The conditions include using DD-AG and DD-LAG with/without light irradiation (130 mW cm^{-2}, 4 min). The infusate concentration normalizes the drug concentrations.

6. Conclusions

In summary, we have developed a biodegradable and biocompatible nanosystem (LAGs) that can be loaded with various combinations of therapeutic payloads to achieve on-demand customizable chemo-phototherapy and trigger an adaptive anti-tumor immunity towards hypoxic GBM. We demonstrate that in the presence of 3D printed hypoxic U87 spheroids, DD-LAGs can induce tumor cell death by enhanced chemo-phototherapy through in-situ oxygen generation and capture and retain the TDPAs resulting in allogenic lymphocyte proliferation. The poor clinical success of traditional strategies to stimulate an effective immune response, such as administering one or several antigens, is due to the tumor heterogeneity within individual patients and among patient populations. In contrast to conventional methods, our innovative approach exposes the immune system to a wide variety of TDPAs released through tumor cell death in a patient-specific manner. This treatment strategy could play a pivotal role in the advancement of personalized medicines. Since LAGs contain materials approved by the US Food and Drug Administration, its translation from bench to bedside is certainly possible. However, before that can become a reality, our study holds few limitations: although the spheroid model may mimic microtumors more closely than monolayer cultures, primary tumor cells both in-vitro and in-vivo may react differently to the proposed treatment. Moreover, the antigen capturing and subsequent induction of anti-tumoural immunity in-vivo needs to be studied. Therefore, this proposed treatment approach needs to be evaluated in primary tumor cells and in-vivo animal models.

7. Experimental Section

Materials: All the reagents, equipment, and materials used in this work are listed in the Supporting Information.

Synthesis of LAs: The synthesis of Light responsive antigen captors (LAs) is discussed in detail in the Supporting Information.

Preparation of DD-LAGs: The fabrication of dual-drug loaded LAGs was achieved through a thin-film hydration method. The fabricated LAs, along with the indicated amount of Nutlin-3a and Protoporphyrin IX, was first dissolved in tetrahydrofuran (THF). The solvent was subsequently evaporated under reduced pressure by rotary evaporation to obtain a thin film. The lipid cake was hydrated with 4 ml of phosphate-buffered saline (PBS) ph7.4, followed by bath sonication for 20 mins at 40°C. The unloaded drugs were removed using 200 nm Polyethersulfone (PES) filters. The number of maleimide groups was determined using the Maleimide Quantification Assay Kit. Concurrently, 238μl of Traut's reagent solution (2mg/ml dissolved in pH 8.0 PBS with 5mM EDTA) was added to 5 ml of Catalase (10mg/ml dissolved in pH 8.0 PBS) and stirred for 1 h in the dark. Unreacted Traut's reagent as removed by centrifugation at 10000 rpm on MWCO 10KDa Vivaspins for 20 mins. Then, the number of thiol groups was determined using Ellman's reagent. A post-insertion method was used to graft the catalase onto the DD-LAs. The prepared DD-LAs solution and thiolated catalase (mal: thiol = 1:0.5) were stirred for 24 hrs in the dark. NUT-LAGs, PpIX-LAGs, DD-LGs, and DD-AGs were fabricated using the same procedure described above, with minor changes.

Characterization of NPs: The particle size, PDI, and zeta potential of the nanosystem were characterized using a NanoBrook90 Plus particle size analyzer (Brookhaven Ltd., USA). The morphology of NPs was evaluated using TEM (Jeol JEM-2010F, Jeol Ltd., Japan). For this purpose, a carbon-coated copper TEM grid (300 mesh, Electron Microscopy Sciences, USA) was used to hold a drop of the suspension and allowed to dry at room temperature, and stained with uranyl acetate for 1 min.

The stability of DD-LAGs was assessed in α-MEM medium containing 10% of FBS. Briefly, the samples were dispersed in the media and shaken at 50 rpm at 37°C. The storage stability of DD-LAGs was studied in PBS at 4°C. At each time point (1, 2, 4, 8, 16 days), samples were withdrawn (200μl) and diluted in 800μl of PBS for measuring the size and PDI.

The absorption and fluorescence spectra for the samples were obtained using a UV-Vis spectrophotometer (UV-1700, Shimadzu Corp., Japan) and Fluorescence spectrophotometer (Cary Eclipse, Agilent technologies, USA), respectively. The circular dichroism spectra of the samples were recorded at room temperature using a circular dichroism spectrometer (J-1500, Jasco Inc., Japan).

Quantification of Nutlin-3a, PpIX, and Catalase: To measure the amount of NUT and PpIX loaded within the micelles, 100μl of the samples were dispersed in 900μl of methanol. A C_{18} column was used for the quantification by reverse-phase high-performance liquid chromatography (HPLC, Agilent 1260, Agilent Technologies, USA) method. For HPLC detection, the mobile phase consisted of HPLC grade methanol and 0.5 M sodium acetate at the ratio of 35:65 v/v. The flow rate was set at 0.8152 ml/min and 0. 35 ml/min, the detection wavelength was 260 nm and 401 nm. Catalase was quantified using the Bradford assay, with catalase as the standard.

Oxygen Generation and Catalytic Activity of DD-LAGs: The catalytic activity of DD-LAGs and free catalase were evaluated using the standard Goth's method. Briefly, free catalase and DD-LAGs were

digested with proteinase K for predetermined time points (10, 20, 30, 60, 90, 180, 360 mins), then incubated with H_2O_2 (50 mM) for 1 min at 37°C, before terminating the reaction by adding ammonium molybdate (32.4 mM). Unreacted H_2O_2 was detected by measuring the absorbance at 400 nm using a microplate reader (Infinite 200 PRO, Tecan, Switzerland). H_2O_2 without free catalase or DD-LAGs under the same conditions was used as the control. The relative catalytic activity was calculated using the following equation:

$$\text{The relative catalytic activity } (\%) = (Abs_{Control} - Abs_{sample})/Abs_{control} \times 100\%$$

Where, $Abs_{Control}$ and Abs_{Sample} refer to the absorbance measured at 400 nm for the control and sample, respectively.

In Vitro Release Studies: The on-demand light-triggered payload release experiments were performed by placing 400µl of DD-LAGs and their non-light responsive counterpart (DD-AGs) into an MWCO 2K Slide-A-Lyzer MINI dialysis device with a 2000 molecular weight cut-off (ThermoFisher Scientific, USA). The samples were dialyzed against 1.4 ml of releasing media, pH 7.4 PBS, and pH 5.0 sodium acetate buffer and incubated at 37°C on a platform shaker at 150 r.p.m. At predetermined intervals (5, 10, 15, 20, 25 hr), the medium was withdrawn (100µl) for analysis and replaced with the same amount of fresh medium to maintain the final volume constant during the release experiment. To measure the light-triggered release, samples were exposed to light (130 mW/cm^2) for 4 mins at the 0h and 8hr time points.

3D printing hypoxic U-87 spheroids (h-U87): For the fabrication of tumor spheroids, a hybrid method consisting of liquid overlay technique and drop-on-demand was utilized. Briefly, U87 were harvested and suspended in α-MEM supplemented with 10% FBS and 1% PS at a cell concentration of (2000 cells/well). 3 mL printing cartridges were then filled with the cell suspension. Using the BIO X™ 3D bioprinter (CELLINK®, Sweden), cell suspensions were then extruded through 25G needles into each well of ultra-low attachment 96 well round-bottomed plates. The extrusion pressure used was 20 kPa, and the extrusion time was set to 1 s. Plates were then centrifuged at 1750 rpm for 10 minutes and first incubated for 6 h in a nitrogen environment and subsequently at 37°C and 5% CO_2 concentration for 24h before further studies.

Biocompatibility of B-LAGs: The biocompatibility of Bare light-responsive antigen capturing oxygen generators (B-LAGs) on 3T3 cells was assessed using the MTS assay (Promega Corp., USA), as described in the Supporting Information.

Evaluation of Anti-cancer activity: To study the in-vitro anti-cancer potential of DD-LAGs, DD-LAs, and free payloads (NUT concentration range 0.25-40 µg/ml) were incubated with 3D hypoxic U-87 spheroids, 2D hypoxic U87 cells, and 2D normoxic U87 cells with/without light irradiation (130 mW/cm^2, 4 mins). Free NUT, free PpIX, and a combination of NUT and PpIX were also examined at concentrations similar to the co-loaded micelles. Cell viability of the 3D hypoxic spheroids was measured using CellTiter-Glo 3D Cell Viability Assay (Promega Corp., USA), and the cell viability of 2D cell cultures was measured using MTS assay.

The free payloads and the nanoparticulate system's anti-cancer activity was visualized using Live/Dead Viability/Cytotoxicity Kit (ThermoFisher, USA). Briefly, h-U87 spheroids were incubated with DD-LAGs (NUT 5µg/ml) for 6 hours with/without light irradiation (130 mW/cm^2, 4 mins). Free NUT, free PpIX, a combination of NUT and PpIX and DD-LAs were tested in concentrations corresponding to the amounts loaded in DD-LAGs. Images were obtained using confocal microscopy (FV1000, Olympus Corp., Japan)

Generation of Reactive Oxygen Species (ROS) of DD-LAGs when exposed light irradiation (130 mW/cm^2, 4 mins) was confirmed using DCFH-DA. ROS generation capability was also evaluated for free payloads and DD-LAs. After incubation with the various treatment groups, the cells were washed thrice with DPBS and then incubated with DCFH-DA for 45 mins in the dark. Similarly, the mitochondrial membrane's damage was evaluated using the JC-1 assay (ThermoFisher Scientific, USA). The positive control group was incubated with CCCP for 5 mins. The control and treated groups were then stained with JC-1 (5µg/ml) for 30 mins. In both the experiments, the cells were washed thrice with DBPS at each step and fixed with 4% formaldehyde before analysis using a confocal microscope.

The extent of apoptosis in h-U87 spheroids was examined using Annexin V-FITC/PI Apoptosis Detection Kit (ThermoFisher Scientific, USA). The h-U87 spheroids were incubated with the different treatment groups at equivalent concentrations with/without light irradiation (130 mW/cm^2, 4 mins) for 6 hours. Spheroids were dissociated to obtain single-cell populations using 0.5% trypsin (100µl). Annexin V-FITC apoptosis detection was performed using flow cytometry (Cytoflex, Beckman Coulter) as per the manufacturer's protocol.

The cell cycle distribution of h-U87 spheroids treated with DD-LAGs with/without light irradiation (130 mW/cm^2, 4 mins) for 6 hours was evaluated. The spheroids were dissociated in the same method as mentioned above. The cells were then fixed using cold ethanol (70%) for 1 hr at 4°C, followed by incubation with RNase A and Propidium iodide (PI) for 30 mins at 37°C in the dark. The stained cells were then analyzed using a flow cytometer. At each step, the cells are washed thrice using Dulbecco's Phosphate Buffered Saline (DPBS).

Surface expression of Immunogenic Cell Death (ICD) Biomarkers was assessed via immune fluorescence. h-U87 cells were treated with free NUT, free PpIX, a combination of NUT and PpIX, DD-LA, and DD-LAGs with/without light irradiation (130 mW/cm^2, 4 mins) at equivalent concentrations for 6 hrs. The cells were then fixed using 4% formaldehyde, permeabilized using 0.1 % Triton-X, and blocked using 1% gelatin. Subsequently, the cells were incubated with an anti-calreticulin antibody for 1 hr at room temperature, followed by incubation with Alexa Fluor 488-conjugated secondary antibody for 1 hr at room temperature and finally analyzed using confocal microscopy. At each step, the cells were washed thrice with DPBS.

Extracellular HMGB1 in serum-free media secreted from the cells treated with different groups were measured using the Human HMGB1 Elisa Kit (Novus Biologicals) by following the manufacturer's protocol.

Cellular Uptake of DD-LAGs: The cellular uptakes of equivalent concentrations of Free PpIX, DD-LAs, and DD-LAGs (PpIX concentration 0.702 µg/ml) were studied using confocal fluorescence microscopy. The cells were treated with different groups for 3h and 6h. After incubation, the cells were fixed using 300 µl of 4% paraformaldehyde for 20 mins, stained with 300µl of Phalloidin-IFluor-488 (Abcam, UK) for 45 mins and 300 µl of DAPI (ThermoFisher Scientific, USA) for 5 mins. The cells were washed thrice with DPBS at each step. For flow cytometry, the treated cells were trypsinized, washed with cold PBS thrice, and immediately analyzed.

Penetration of DD-LAGs into h-U87 Spheroids: h-U87 spheroids were treated with the same concentrations of free PpIX, DD-LAs, and DD-LAGs as in the cell uptake study for 6 hr. The spheroids were fixed with 100 µl of 4% paraformaldehyde for 20 mins, permeabilized using 100 µl of 0.1 % Triton-X for 10 mins, dehydrated, and rehydrated using cold methanol (0, 25, 50, 75, 100 %) for 10

mins each. The spheroids were incubated with 10 µl of CytoVista 3D cell culture clearing reagent (ThermoFisher Scientific, USA).

Effects of endocytosis inhibitors on the penetration of DD-LAGs: The h-U87 spheroids were pre-treated with a caveolae inhibitor, genistein, or Exo1 at concentrations of 200 µM and 50 µM respectively for 1 h. Afterward, the DD-LAGs (NUT concentration 5 µg/ml) was added to the spheroids and incubated for 6 h. The spheroids were washed thrice with DPBS and observed by confocal microscopy.

Intracellular trafficking of DD-LAGs in h-U87 cells: The h-U87 cells were treated with DD-LAGs for 6 h, then the macropinosomes were labeled by 70 kDa^{RhoB}dextran (250 µg/ml) for 45 mins, lysosomes were stained with LysoTracker Green (50 nM) for 45 mins, Golgi and Endoplasmic Reticulum were marked with Golgi Staining Kit Green and ER Staining Kit Green respectively, according to the manufacturer's instructions. A confocal laser scanning microscope was used to capture the images.

Effects of endocytosis inhibitors on cellular uptake of DD-LAGs: The cells treated with DD-LAGs for 6 h were washed thrice with DPBS, and the medium was replaced with fresh medium, and subsequently, four endocytosis inhibitors (dynasore, genistein, chlorpromazine, wortmannin) were added separately into the cell culture medium at concentrations of 50 µM, 50 µM, 100 µM, and 25 µM respectively. The cells were fixed and analyzed using confocal microscopy. For flow cytometry, the cells were trypsinized and washed with DPBS, and the fluorescence intensity in each group was quantitatively determined using flow cytometry. The cells were washed thrice with DPBS at each step.

Transcellular delivery of DD-LAGs: h-U87 cells were seeded on coverslips (i)-(iii) and allowed to attach for 24 h. The cells on the coverslip (i) were incubated with DD-LAGs (NUT concentration 5 µg/ml) for 4 h. The cells on the coverslip (i) were washed with DPBS thrice and co-cultured with fresh h-U87 cells grown on the coverslip (ii) in a fresh medium for 12 h. The cells on the coverslip (ii) were then taken, washed thrice with DPBS, and co-cultured with fresh cells on the coverslip (iii) in a fresh culture medium for another 12 h. Before imaging on a confocal microscope, the cells were fixed and stained with DAPI.

Antigen Capturing Ability of DD-LAGs: The h-U87 cells were incubated with NUT and PpIX for 4h, the cells were then washed with DPBS thrice and exposed to light irradiation (130 mW/cm^2, 4 mins). Subsequently, the cells were incubated in serum-free media for 24 h. After incubation, the supernatant was collected and centrifuged at 300 g for 5 min to remove the insoluble cellular debris. DD-LAGs and their non-antigen capturing analogues (DD-LGs) were incubated with antigen containing supernatants for 24 h. The particle size and zeta potential of DD-LAGs and DD-LGs were measured before and after incubation.

Dendritic Cell Stimulation: The capacity of DD-LAGs to elicit DC maturation was studied using flow cytometry. Initially, 1 x 10^5 Mo-DCs/well were seeded in 24 well plates and incubated for at 37°C for 24 h with DD-LAGs (NUT concentration 5 µg/ml). Similarly, free NUT, free PpIX, a combination of NUT and PpIX, and DD-LAs, in concentrations correspondent to the amounts loaded in DD-LAGs. The control group was treated with 50 ng/ml TNF-α and 50 ng/ml IL-1β for 24 hr. The cell suspensions were then collected and centrifuged at 300 g for 5 mins. After discarding the supernatant, the cells were re-suspended in cold DPBS (100 µl) containing anti-CD83 (1 µl) and anti-CD83 (1 µl) and incubated at 4°C for 15 min. The cells were subsequently washed with cold DPBS thrice and centrifuged at 300 g for 5 min to remove unbound antibodies. Finally, the cells were re-suspended in

cold DPBS (100 µl) containing 7-AAD (2 µl) and incubated for 10 min in the dark. The cells were then analyzed using a flow cytometer.

T-cell differentiation and proliferation: CellTrace Violet Cell Proliferation (5 x 10^{-6} M) was used to label the previously isolated CD14$^-$ cells by incubating at room temperature for 15 min in the dark. The cells were then washed thrice with RPMI + 10% FBS. The labeled cells were then re-suspended in RPMI + 10% FBS. The allogenic stimulated Mo-DCs, as described above, were added to each well at a concentration of 1 x 10^5 cells/ml. The labeled CD14$^-$ cells were added to the well containing the Mo-DCs at a concentration of 1 x 10^6 cells/ml (Mo-DCs: CD14$^-$, 1:10) and incubated at 37°C for 24 h. The cell suspensions were centrifuged and washed with cold DBPS thrice. As described above, staining with specific T cells markers and 7-AAD was achieved using the same procedure for DC stimulation. The cells were re-suspended in cold DBPS (100 µl) containing anti-CD3 (1 µl), anti-CD4 (1 µl) and anti-CD8 (1 µl). The samples were analyzed using a flow cytometer.

Effect on adaptive immunity due to h-U87 Spheroid and DC Coculture: 250 h-U87 spheroids per well were added to ultra-low attachment 24-well plates and incubated with free NUT, free PpIX, a combination of NUT and PpIX, DD-LAs and DD-LAGs (NUT concentration 5 µg/ml) with/without light irradiation (130 mW/cm^2, 4 mins) for 24 hr, at equivalent concentrations. The spheroids were washed thrice with DPBS and co-incubated with 1 x 10^5 Mo-DCs for 24 h. Subsequently, the cells in suspension were centrifuged, and the supernatants were stored for further analysis of secreted cytokines.

For DC stimulation, the cells were labeled with anti-CD83, anti-CD86, and 7-AAD using the same protocol mentioned above and analyzed using flow cytometry. The cells in suspension were filtered through a 100 nm filter to remove the spheroids before analysis.

To study the T-cell proliferation, the cells were co-cultured with CellTrace Violet labeled autologous 1 x 10^6 CD14$^-$ cells for a further 24 hr. Finally, the cells were stained with anti-CD3, anti-CD4, anti-CD8, and 7-AAD as described above and analyzed using a flow cytometer.

Model formulation: The mathematical models consist of governing equations for the transport of PpIX and NUT in the nanoparticle-encapsulated form and free form between different tissue compartments, including tumor extracellular space (ECS), tumor intracellular space (ICS), and intravascular space (IVS), as well as equations describing the immunotherapy and chemotherapy efficacy. Similar models have been reported previously with applications in predicting the performances of different drugs [84, 87, 88]. A summary of the mathematical equations and model parameters is given in the Supporting Information.

The dynamics processes in drug delivery include drug release from nanoparticles, drug exchange between IVS and ECS, and influx and efflux of drugs from ECS to ICS. The effect of immunotherapy is determined by natural killer cells, CD8+ cells, and lymphocytes cells, whose concentrations are subject to the drug IVS concentrations. The drug release in IVS, tumor ECS, and ICS are simulated, depending on the local pH value and the release condition (with or without light projection).

Statistical Analysis: Data were calculated and processed as mean ± standard deviation (SD) of at least three independent experiments. Comparison between groups was analyzed with Student's t-test. Statistical differences were considered significant at *$p < 0.05$, **$p < 0.01$, ***$p < 0.001$.

Credit Author Statement

Vishnu Sunil: Conceptualization, Methodology, Investigation, Data Curation, Writing – Original Draft. Anbu Mozhi: Methodology, Investigation (H&E staining, TUNEL assay). Wenbo Zhan: Methodology, Formal Analysis, Investigation. Jia Heng Teoh: Methodology, Investigation (3D printing). Chi-Hwa Wang – Conceptualization, Supervision, Writing – Review and Editing, Funding Acquisition.

Declaration of Competing Interests

The authors declare that they have no known competing financial interests or personal relationships that could have appeared to influence the work reported in this paper.

Acknowledgments

Data availability statement

The raw data required to reproduce these findings are available upon request from the corresponding author of this manuscript.

References

[1] S. Mallick, R. Benson, A. Hakim, G.K. Rath, Management of glioblastoma after recurrence: A changing paradigm, Journal of the Egyptian National Cancer Institute 28(4) (2016) 199-210.

[2] C. Alifieris, D.T. Trafalis, Glioblastoma multiforme: Pathogenesis and treatment, Pharmacology & therapeutics 152 (2015) 63-82.

[3] P. Kadiyala, D. Li, F.M. Nuñez, D. Altshuler, R. Doherty, R. Kuai, M. Yu, N. Kamran, M. Edwards, J.J. Moon, High-density lipoprotein-mimicking nanodiscs for chemo-immunotherapy against glioblastoma multiforme, ACS nano 13(2) (2019) 1365-1384.

[4] L. Zhang, J.R. Conejo-Garcia, D. Katsaros, P.A. Gimotty, M. Massobrio, G. Regnani, A. Makrigiannakis, H. Gray, K. Schlienger, M.N. Liebman, Intratumoral T cells, recurrence, and survival in epithelial ovarian cancer, New England journal of medicine 348(3) (2003) 203-213.

[5] O. Nakano, M. Sato, Y. Naito, K. Suzuki, S. Orikasa, M. Aizawa, Y. Suzuki, I. Shintaku, H. Nagura, H. Ohtani, Proliferative activity of intratumoral CD8+ T-lymphocytes as a prognostic factor in human renal cell carcinoma: clinicopathologic demonstration of antitumor immunity, Cancer research 61(13) (2001) 5132-5136.

[6] K. Schumacher, W. Haensch, C. Röefzaad, P.M. Schlag, Prognostic significance of activated CD8+ T cell infiltrations within esophageal carcinomas, Cancer research 61(10) (2001) 3932-3936.

[7] N.A. Wages, C. Chiuzan, K.S. Panageas, Design considerations for early-phase clinical trials of immune-oncology agents, Journal for immunotherapy of cancer 6(1) (2018) 81.

[8] L. Zitvogel, L. Galluzzi, M.J. Smyth, G. Kroemer, Mechanism of action of conventional and targeted anticancer therapies: reinstating immunosurveillance, Immunity 39(1) (2013) 74-88.

[9] D.M. Pardoll, The blockade of immune checkpoints in cancer immunotherapy, Nature Reviews Cancer 12(4) (2012) 252-264.

[10] S.L. Topalian, F.S. Hodi, J.R. Brahmer, S.N. Gettinger, D.C. Smith, D.F. McDermott, J.D. Powderly, R.D. Carvajal, J.A. Sosman, M.B. Atkins, Safety, activity, and immune correlates of anti–PD-1 antibody in cancer, New England Journal of Medicine 366(26) (2012) 2443-2454.

[11] F. Yi, N. Frazzette, A.C. Cruz, C.A. Klebanoff, R.M. Siegel, Beyond cell death: new functions for TNF family cytokines in autoimmunity and tumor immunotherapy, Trends in molecular medicine 24(7) (2018) 642-653.

[12] V. Golubovskaya, CAR-T cell therapy: from the bench to the bedside, Multidisciplinary Digital Publishing Institute, 2017.

[13] L. DeFrancesco, CAR-T cell therapy seeks strategies to harness cytokine storm, Nature Publishing Group, 2014.

[14] L. Zitvogel, O. Kepp, G. Kroemer, Immune parameters affecting the efficacy of chemotherapeutic regimens, Nature reviews Clinical oncology 8(3) (2011) 151.

[15] J.H. Sampson, K.D. Aldape, G.E. Archer, A. Coan, A. Desjardins, A.H. Friedman, H.S. Friedman, M.R. Gilbert, J.E. Herndon, R.E. McLendon, Greater chemotherapy-induced lymphopenia enhances tumor-specific immune responses that eliminate EGFRvIII-expressing tumor cells in patients with glioblastoma, Neuro-oncology 13(3) (2011) 324-333.

[16] J.F. Kerr, A.H. Wyllie, A.R. Currie, Apoptosis: a basic biological phenomenon with wideranging implications in tissue kinetics, British journal of cancer 26(4) (1972) 239-257.

[17] S. Kim, K.B. Elkon, X. Ma, Transcriptional suppression of interleukin-12 gene expression following phagocytosis of apoptotic cells, Immunity 21(5) (2004) 643-653.

[18] R.M. Steinman, S. Turley, I. Mellman, K. Inaba, The induction of tolerance by dendritic cells that have captured apoptotic cells, The Journal of experimental medicine 191(3) (2000) 411-416.

[19] P. Rovere, M.G. Sabbadini, C. Vallinoto, U. Fascio, V.S. Zimmermann, A. Bondanza, P. Ricciardi-Castagnoli, A.A. Manfredi, Delayed clearance of apoptotic lymphoma cells allows cross-presentation of intracellular antigens by mature dendritic cells, Journal of leukocyte biology 66(2) (1999) 345-349.

[20] P. Wijermans, W. Gerrits, H. Haak, Severe immunodeficiency in patients treated with fludarabine monophosphate, European journal of haematology 50(5) (1993) 292-296.

[21] A.J. Lumsden, J.P. Codde, B.N. Gray, P.H. Van der Meide, Prevention of myelosuppression does not improve the therapeutic efficacy of chemo-immunotherapy, Anticancer Res 12(5) (1992) 1725-1729.

[22] J.N. Barreto, K.B. McCullough, L.L. Ice, J.A. Smith, Antineoplastic agents and the associated myelosuppressive effects: a review, Journal of pharmacy practice 27(5) (2014) 440-446.

[23] L. Galluzzi, A. Buqué, O. Kepp, L. Zitvogel, G. Kroemer, Immunogenic cell death in cancer and infectious disease, Nature Reviews Immunology 17(2) (2017) 97.

[24] D.R. Green, T. Ferguson, L. Zitvogel, G. Kroemer, Immunogenic and tolerogenic cell death, Nature Reviews Immunology 9(5) (2009) 353-363.

[25] D. Liu, B. Chen, Y. Mo, Z. Wang, T. Qi, Q. Zhang, Y. Wang, Redox-Activated Porphyrin-Based Liposome Remote-Loaded with Indoleamine 2, 3-Dioxygenase (IDO) Inhibitor for Synergistic Photoimmunotherapy through Induction of Immunogenic Cell Death and Blockage of IDO Pathway, Nano letters 19(10) (2019) 6964-6976.

[26] M. Obeid, A. Tesniere, F. Ghiringhelli, G.M. Fimia, L. Apetoh, J.-L. Perfettini, M. Castedo, G. Mignot, T. Panaretakis, N. Casares, Calreticulin exposure dictates the immunogenicity of cancer cell death, Nature medicine 13(1) (2007) 54-61.

[27] S. Lim, J. Park, M.K. Shim, W. Um, H.Y. Yoon, J.H. Ryu, D.-K. Lim, K. Kim, Recent advances and challenges of repurposing nanoparticle-based drug delivery systems to enhance cancer immunotherapy, Theranostics 9(25) (2019) 7906.

[28] C. Xia, S. Yin, S. Xu, G. Ran, M. Deng, L. Mei, X. Tang, J. Rao, M. Li, Z. Zhang, Low Molecular Weight Heparin-Coated and Dendrimer-Based Core-Shell Nanoplatform with Enhanced Immune Activation and Multiple Anti-Metastatic Effects for Melanoma Treatment, Theranostics 9(2) (2019) 337.

[29] J. Laengle, J. Stift, A. Bilecz, B. Wolf, A. Beer, B. Hegedus, S. Stremitzer, P. Starlinger, D. Tamandl, D. Pils, DNA damage predicts prognosis and treatment response in colorectal liver metastases superior to immunogenic cell death and T cells, Theranostics 8(12) (2018) 3198.

[30] T.N. Schumacher, R.D. Schreiber, Neoantigens in cancer immunotherapy, Science 348(6230) (2015) 69-74.

[31] P. Vaupel, O. Thews, M. Hoeckel, Treatment resistance of solid tumors, Medical oncology 18(4) (2001) 243-259.

[32] X. Song, J. Xu, C. Liang, Y. Chao, Q. Jin, C. Wang, M. Chen, Z. Liu, Self-supplied tumor oxygenation through separated liposomal delivery of H_2O_2 and catalase for enhanced radio-immunotherapy of cancer, Nano letters 18(10) (2018) 6360-6368.

[33] O. Trédan, C.M. Galmarini, K. Patel, I.F. Tannock, Drug resistance and the solid tumor microenvironment, Journal of the National Cancer Institute 99(19) (2007) 1441-1454.

[34] P. Vaupel, Tumor microenvironmental physiology and its implications for radiation oncology, Seminars in radiation oncology, Elsevier, 2004, pp. 198-206.

[35] H. Harada, How can we overcome tumor hypoxia in radiation therapy?, Journal of radiation research 52(5) (2011) 545-556.

[36] S. Thomas, M.A. Harding, S.C. Smith, J.B. Overdevest, M.D. Nitz, H.F. Frierson, S.A. Tomlins, G. Kristiansen, D. Theodorescu, CD24 is an effector of HIF-1–driven primary tumor growth and metastasis, Cancer research 72(21) (2012) 5600-5612.

[37] R. Noy, J.W. Pollard, Tumor-associated macrophages: from mechanisms to therapy, Immunity 41(1) (2014) 49-61.

[38] T. Chanmee, P. Ontong, K. Konno, N. Itano, Tumor-associated macrophages as major players in the tumor microenvironment, Cancers 6(3) (2014) 1670-1690.

[39] A.-T. Henze, M. Mazzone, The impact of hypoxia on tumor-associated macrophages, The Journal of clinical investigation 126(10) (2016) 3672-3679.

[40] G. Song, C. Liang, X. Yi, Q. Zhao, L. Cheng, K. Yang, Z. Liu, Perfluorocarbon-loaded hollow Bi2Se3 nanoparticles for timely supply of oxygen under near-infrared light to enhance the radiotherapy of cancer, Advanced materials 28(14) (2016) 2716-2723.

[41] Y. Cheng, H. Cheng, C. Jiang, X. Qiu, K. Wang, W. Huan, A. Yuan, J. Wu, Y. Hu, Perfluorocarbon nanoparticles enhance reactive oxygen levels and tumour growth inhibition in photodynamic therapy, Nature communications 6(1) (2015) 1-8.

[42] D.-W. Zheng, B. Li, C.-X. Li, J.-X. Fan, Q. Lei, C. Li, Z. Xu, X.-Z. Zhang, Carbon-dot-decorated carbon nitride nanoparticles for enhanced photodynamic therapy against hypoxic tumor via water splitting, ACS nano 10(9) (2016) 8715-8722.

[43] S. Wang, F. Yuan, K. Chen, G. Chen, K. Tu, H. Wang, L.-Q. Wang, Synthesis of hemoglobin conjugated polymeric micelle: a ZnPc carrier with oxygen self-compensating ability for photodynamic therapy, Biomacromolecules 16(9) (2015) 2693-2700.

[44] W. Fan, W. Bu, B. Shen, Q. He, Z. Cui, Y. Liu, X. Zheng, K. Zhao, J. Shi, Intelligent MnO2 Nanosheets Anchored with Upconversion Nanoprobes for Concurrent pH-/H2O2-Responsive UCL Imaging and Oxygen-Elevated Synergetic Therapy, Advanced materials 27(28) (2015) 4155-4161.

[45] X. Li, N. Kwon, T. Guo, Z. Liu, J. Yoon, Innovative strategies for hypoxic-tumor photodynamic therapy, Angewandte Chemie International Edition 57(36) (2018) 11522-11531.

[46] H. Gong, Y. Chao, J. Xiang, X. Han, G. Song, L. Feng, J. Liu, G. Yang, Q. Chen, Z. Liu, Hyaluronidase to enhance nanoparticle-based photodynamic tumor therapy, Nano letters 16(4) (2016) 2512-2521.

[47] C.-C. Huang, W.-T. Chia, M.-F. Chung, K.-J. Lin, C.-W. Hsiao, C. Jin, W.-H. Lim, C.-C. Chen, H.-W. Sung, An implantable depot that can generate oxygen in situ for overcoming hypoxia-induced resistance to anticancer drugs in chemotherapy, Journal of the American Chemical Society 138(16) (2016) 5222-5225.

[48] R. Zhang, X. Song, C. Liang, X. Yi, G. Song, Y. Chao, Y. Yang, K. Yang, L. Feng, Z. Liu, Catalase-loaded cisplatin-prodrug-constructed liposomes to overcome tumor hypoxia for enhanced chemo-radiotherapy of cancer, Biomaterials 138 (2017) 13-21.

[49] S. Wilhelm, A.J. Tavares, Q. Dai, S. Ohta, J. Audet, H.F. Dvorak, W.C. Chan, Analysis of nanoparticle delivery to tumours, Nature reviews materials 1(5) (2016) 1-12.

[50] P.P. Wang, J. Frazier, H. Brem, Local drug delivery to the brain, Advanced drug delivery reviews 54(7) (2002) 987-1013.

[51] D. Allhenn, M.A.S. Boushehri, A. Lamprecht, Drug delivery strategies for the treatment of malignant gliomas, International journal of pharmaceutics 436(1-2) (2012) 299-310.

[52] D. Yin, Y. Zhai, H.E. Gruber, C.E. Ibanez, J.M. Robbins, A.P. Kells, N. Kasahara, J. Forsayeth, D.J. Jolly, K.S. Bankiewicz, Convection-enhanced delivery improves distribution and efficacy of tumor-selective retroviral replicating vectors in a rodent brain tumor model, Cancer gene therapy 20(6) (2013) 336-341.

[53] M. Van Woensel, N. Wauthoz, R. Rosière, K. Amighi, V. Mathieu, F. Lefranc, S.W. Van Gool, S. De Vleeschouwer, Formulations for intranasal delivery of pharmacological agents to combat brain disease: a new opportunity to tackle GBM?, Cancers 5(3) (2013) 1020-1048.

[54] W. Zhan, C.-H. Wang, Convection enhanced delivery of chemotherapeutic drugs into brain tumour, Journal of Controlled Release 271 (2018) 74-87.

[55] W. Zhan, C.-H. Wang, Convection enhanced delivery of liposome encapsulated doxorubicin for brain tumour therapy, Journal of Controlled Release 285 (2018) 212-229.

[56] G. Guo, Y. Cui, New perspective on targeting the tumor suppressor p53 pathway in the tumor microenvironment to enhance the efficacy of immunotherapy, Journal for immunotherapy of cancer 3(1) (2015) 9.

[57] G. Guo, M. Yu, W. Xiao, E. Celis, Y. Cui, Local activation of p53 in the tumor microenvironment overcomes immune suppression and enhances antitumor immunity, Cancer research 77(9) (2017) 2292-2305.

[58] C. Gasparini, A. Tommasini, G. Zauli, The MDM2 inhibitor Nutlin-3 modulates dendritic cell–induced T cell proliferation, Human immunology 73(4) (2012) 342-345.

[59] A. Mozhi, V. Sunil, W. Zhan, P.B. Ghode, N.V. Thakor, C.-H. Wang, Enhanced penetration of pro-apoptotic and anti-angiogenic micellar nanoprobe in 3D multicellular spheroids for chemophototherapy, Journal of Controlled Release (2020).

[60] C. Zhao, H. Deng, J. Xu, S. Li, L. Zhong, L. Shao, Y. Wu, X.-j. Liang, "Sheddable" PEG-lipid to balance the contradiction of PEGylation between long circulation and poor uptake, Nanoscale 8(20) (2016) 10832-10842.

[61] K. Zhang, X. Tang, J. Zhang, W. Lu, X. Lin, Y. Zhang, B. Tian, H. Yang, H. He, PEG–PLGA copolymers: Their structure and structure-influenced drug delivery applications, Journal of Controlled release 183 (2014) 77-86.

[62] T.L. Moore, L. Rodriguez-Lorenzo, V. Hirsch, S. Balog, D. Urban, C. Jud, B. Rothen-Rutishauser, M. Lattuada, A. Petri-Fink, Nanoparticle colloidal stability in cell culture media and impact on cellular interactions, Chemical Society Reviews 44(17) (2015) 6287-6305.

[63] L. Shen, Y. Huang, D. Chen, F. Qiu, C. Ma, X. Jin, X. Zhu, G. Zhou, Z. Zhang, pH-responsive aerobic nanoparticles for effective photodynamic therapy, Theranostics 7(18) (2017) 4537.

[64] S. Moreno-Pérez, A. Orrego, M. Romero-Fernández, L. Trobo-Maseda, S. Martins-DeOliveira, R. Munilla, G. Fernández-Lorente, J. Guisan, Intense PEGylation of enzyme surfaces: relevant stabilizing effects, Methods in enzymology 571 (2016) 55-72.

[65] S. Schöttler, G. Becker, S. Winzen, T. Steinbach, K. Mohr, K. Landfester, V. Mailänder, F.R. Wurm, Protein adsorption is required for stealth effect of poly (ethylene glycol)-and poly (phosphoester)-coated nanocarriers, Nature nanotechnology 11(4) (2016) 372-377.

[66] S. Riffle, R.S. Hegde, Modeling tumor cell adaptations to hypoxia in multicellular tumor spheroids, Journal of Experimental & Clinical Cancer Research 36(1) (2017) 102.

[67] S. Al Habyan, C. Kalos, J. Szymborski, L. McCaffrey, Multicellular detachment generates metastatic spheroids during intra-abdominal dissemination in epithelial ovarian cancer, Oncogene 37(37) (2018) 5127-5135.

[68] F. Gao, J. Yi, J.Q. Yuan, G.Y. Shi, X.M. Tang, The cell cycle related apoptotic susceptibility to arsenic trioxide is associated with the level of reactive oxygen species, Cell research 14(1) (2004) 81-85.

[69] R. Villalonga-Planells, L. Coll-Mulet, F. Martínez-Soler, E. Castaño, J.-J. Acebes, P. Giménez-Bonafé, J. Gil, A. Tortosa, Activation of p53 by nutlin-3a induces apoptosis and cellular senescence in human glioblastoma multiforme, PloS one 6(4) (2011) e18588.

[70] B. Wang, L. Fang, H. Zhao, T. Xiang, D. Wang, MDM2 inhibitor Nutlin-3a suppresses proliferation and promotes apoptosis in osteosarcoma cells, Acta Biochim Biophys Sin 44(8) (2012) 685-691.

[71] T. Nonaka, A. Nanashima, M. Nonaka, M. Uehara, H. Isomoto, I. Asahina, T. Nagayasu, Analysis of apoptotic effects induced by photodynamic therapy in a human biliary cancer cell line, Anticancer Res 30(6) (2010) 2113-2118.

[72] S. Kumari, M. Swetha, S. Mayor, Endocytosis unplugged: multiple ways to enter the cell, Cell research 20(3) (2010) 256-275.

[73] S.G. Aller, J. Yu, A. Ward, Y. Weng, S. Chittaboina, R. Zhuo, P.M. Harrell, Y.T. Trinh, Q. Zhang, I.L. Urbatsch, Structure of P-glycoprotein reveals a molecular basis for poly-specific drug binding, Science 323(5922) (2009) 1718-1722.

[74] Y. Min, K.C. Roche, S. Tian, M.J. Eblan, K.P. McKinnon, J.M. Caster, S. Chai, L.E. Herring, L. Zhang, T. Zhang, Antigen-capturing nanoparticles improve the abscopal effect and cancer immunotherapy, Nature nanotechnology 12(9) (2017) 877.

[75] A. Shahinian, K. Pfeffer, K.P. Lee, T.M. Kundig, K. Kishihara, A. Wakeham, K. Kawai, P.S. Ohashi, C.B. Thompson, T.W. Mak, Differential T cell costimulatory requirements in CD28-deficient mice, Science 261(5121) (1993) 609-612.

[76] J. Zheng, Q. Liu, J. Yang, Q. Ren, W. Cao, J. Yang, Z. Yu, F. Yu, Y. Wu, H. Shi, Co-culture of apoptotic breast cancer cells with immature dendritic cells: a novel approach for DC-based vaccination in breast cancer, Brazilian Journal of Medical and Biological Research 45(6) (2012) 510-515.

[77] M.J. Seo, G.R. Kim, Y.M. Son, D.-C. Yang, H. Chu, T.S. Min, I.D. Jung, Y.-M. Park, S.H. Han, C.-H. Yun, Interactions of dendritic cells with cancer cells and modulation of surface molecules affect functional properties of CD8+ T cells, Molecular immunology 48(15-16) (2011) 1744-1752.

[78] O. Bloch, C.A. Crane, R. Kaur, M. Safaee, M.J. Rutkowski, A.T. Parsa, Gliomas promote immunosuppression through induction of B7-H1 expression in tumor-associated macrophages, Clinical cancer research 19(12) (2013) 3165-3175.

[79] A. O'Garra, F.J. Barrat, A.G. Castro, A. Vicari, C. Hawrylowicz, Strategies for use of IL-10 or its antagonists in human disease, Immunological reviews 223(1) (2008) 114-131.

[80] E. Voronov, S. Dotan, Y. Krelin, X. Song, M. Elkabets, Y. Carmi, P. Rider, I. Cohen, M. Romzova, I. Kaplanov, Unique versus redundant functions of IL-1α and IL-1β in the tumor microenvironment, Frontiers in immunology 4 (2013) 177.

[81] S.Z. Ben-Sasson, J. Hu-Li, J. Quiel, S. Cauchetaux, M. Ratner, I. Shapira, C.A. Dinarello, W.E. Paul, IL-1 acts directly on CD4 T cells to enhance their antigen-driven expansion and differentiation, Proceedings of the National Academy of Sciences 106(17) (2009) 7119-7124.

[82] M.-A. Shahbazi, T.D. Fernández, E.M. Mäkilä, X. Le Guével, C. Mayorga, M.H. Kaasalainen, J.J. Salonen, J.T. Hirvonen, H.A. Santos, Surface chemistry dependent immunostimulative potential of porous silicon nanoplatforms, Biomaterials 35(33) (2014) 9224-9235.

[83] T.L. Slatter, M. Wilson, C. Tang, H.G. Campbell, V.K. Ward, V.L. Young, D. Van Ly, N.I. Fleming, A.W. Braithwaite, M.A. Baird, Antitumor cytotoxicity induced by bone-marrow-derived antigen-presenting cells is facilitated by the tumor suppressor protein p53 via regulation of IL-12, Oncoimmunology 5(3) (2016) e1112941.

[84] W. Zhan, W. Gedroyc, X. Yun Xu, Mathematical modelling of drug transport and uptake in a realistic model of solid tumour, Protein and peptide letters 21(11) (2014) 1146-1156.

[85] C. Liu, J. Krishnan, X.Y. Xu, Intrinsic and induced drug resistance mechanisms: in silico investigations at the cellular and tissue scales, Integrative Biology 7(9) (2015) 1044-1060.

[86] Y. Mardor, Y. Roth, Z. Lidar, T. Jonas, R. Pfeffer, S.E. Maier, M. Faibel, D. Nass, M. Hadani, A. Orenstein, Monitoring response to convection-enhanced taxol delivery in brain tumor patients using diffusion-weighted magnetic resonance imaging, Cancer research 61(13) (2001) 4971-4973.

[87] C. Wilhelm, F. Gazeau, J. Roger, J. Pons, J.-C. Bacri, Interaction of anionic superparamagnetic nanoparticles with cells: kinetic analyses of membrane adsorption and subsequent internalization, Langmuir 18(21) (2002) 8148-8155.

[88] L.G. de Pillis, W. Gu, A.E. Radunskaya, Mixed immunotherapy and chemotherapy of tumors: modeling, applications and biological interpretations, Journal of theoretical biology 238(4) (2006) 841-862.

Declaration of interests

☒ The authors declare that they have no known competing financial interests or personal relationships that could have appeared to influence the work reported in this paper.

☐The authors declare the following financial interests/personal relationships which may be considered as potential competing interests: